

Optimal and Model Predictive Control of Cardiac Alternans

by

Felicia Marella Yapari

A thesis submitted in partial fulfillment of the requirements for the degree of

Master of Science

in

Process Control

Department of Chemical and Materials Engineering  
University of Alberta

© Felicia Marella Yapari, 2014

# Abstract

The presence of alternans, which is a persistent alternation in the cardiac action potential duration, has been linked to the onset of ventricular arrhythmia, which may lead to sudden cardiac death. In this thesis, we examine the problem of alternans annihilation in a 1D cable of cardiac cells using optimal and model predictive control strategies, through boundary and spatially distributed actuations. In the first part of the thesis, the system of parabolic partial differential equations (PDEs) describing the small amplitude of alternans and the alternation of peak intracellular  $\text{Ca}^{2+}$  concentration are stabilized by optimal full state feedback control. A model predictive controller (MPC) was then formulated for the small amplitude of alternans PDE. Finally, to address the issue of controller robustness with respect to model uncertainties, a robust MPC was implemented on the small amplitude of alternans PDE. Simulation studies for all three control methods demonstrate that the proposed strategies can successfully annihilate alternans in cables that are significantly longer than 1 cm, thus overcoming the limitations of earlier control efforts.

# Preface

Chapter 2 of this thesis is an edited version of F. Yapari, D. Deshpande, Y. Belhamadia and S. Dubljevic, "Control of Cardiac Alternans by Mechanical and Electrical Feedback," *Physical Review E*, vol. 90, 012706, 2014. Copyright (2014) by the American Physical Society. Sections 1 to 3 of this publication are included in this thesis. For these sections, I was responsible for performing the problem analysis, numerical simulation and manuscript composition. Dr. S. Dubljevic and Dr. Y. Belhamadia were the supervisory authors and were involved with concept formation and manuscript composition.

Chapter 3 of this thesis is a version of F. Yapari and S. Dubljevic, "Model Predictive Control of the Cardiac Amplitude of Alternans PDE," *Proceedings of the 2014 American Control Conference (ACC)*. IEEE, 2014, pp. 5440-5445. Copyright (2014) IEEE. I was responsible for performing the problem analysis, numerical simulation and manuscript composition. Dr. S. Dubljevic was the supervisory author and was involved with concept formation and manuscript composition. In reference to IEEE copyrighted material which is used with permission in this thesis, the IEEE does not endorse any of University of Alberta's products or services.

# Acknowledgements

I would like to thank my supervisors, Dr. Stevan Dubljevic and Dr. Youssef Belhamadia for the guidance and support in the past two years, and for giving me the freedom to pursue my interests. I really appreciate all the insightful discussions that we have had, which helped me immensely in understanding the project.

To my family, thank you for believing in me and for encouraging me to pursue this path. I would not have made it this far without your support and understanding.

Finally, to all my friends, thank you for being there for me. Even though I have not seen some of you in many years, I am glad that we still manage to stay in touch after all these years. I am truly grateful for each and every one of you.

# Contents

<b>1</b>	<b>Introduction</b>	<b>1</b>
1.1	Motivation . . . . .	1
1.2	Background . . . . .	2
1.2.1	The control problem . . . . .	3
1.3	Thesis outline and contributions . . . . .	5
<b>2</b>	<b>Optimal control of cardiac alternans</b>	<b>7</b>
2.1	Introduction . . . . .	7
2.2	Model description . . . . .	8
2.2.1	State space system representation . . . . .	10
2.3	Optimal controller formulation . . . . .	15
2.4	Numerical simulation . . . . .	16
2.4.1	Case 1: LR1 ionic model . . . . .	18
2.4.2	Case 2: Fox ionic model . . . . .	19
2.5	Conclusion . . . . .	23
<b>3</b>	<b>Model predictive control of the amplitude of alternans PDE</b>	<b>24</b>
3.1	Introduction . . . . .	24
3.2	Model description . . . . .	25
3.2.1	State space system representation . . . . .	26
3.3	Model Predictive Control . . . . .	28
3.3.1	Controller formulation . . . . .	29
3.3.2	Constraints . . . . .	30
3.4	Numerical Simulation . . . . .	32
3.5	Conclusion . . . . .	37

<b>4</b>	<b>Robust model predictive control of the amplitude of alternans PDE</b>	<b>38</b>
4.1	Introduction . . . . .	38
4.2	Model description . . . . .	39
4.2.1	Polytopic model for the uncertain system . . . . .	40
4.3	Robust model predictive control . . . . .	40
4.4	Numerical Simulation . . . . .	43
4.5	Conclusion . . . . .	48
<b>5</b>	<b>Conclusions and future work</b>	<b>49</b>
5.1	Conclusions . . . . .	49
5.2	Future work . . . . .	50
	<b>Bibliography</b>	<b>52</b>

# List of Tables

2.1	PDE parameter values for the LR1 and Fox ionic models . . . . .	16
4.1	Combination of parameters for the uncertain models, in terms of deviation from the nominal values . . . . .	44

# List of Figures

1.1	Time evolution of transmembrane potential (black) and intracellular calcium concentration (red) in the presence of alternans. APD and DI correspond to systolic (high) and diastolic (low) blood pressures. . . . .	2
1.2	Intracellular $[Ca^{2+}]$ dynamics . . . . .	5
2.1	Restitution curve for the Fox ionic model obtained using an S1 period of 350 ms and S2 periods ranging from 340 to 200 ms. . . . .	9
2.2	Eigenspectrum of $\mathcal{A}^e$ for the LR1 model, for different cable lengths. . . . .	17
2.3	Eigenspectrum of $\mathcal{A}^e$ for the Fox ionic model, for different cable lengths. . . . .	17
2.4	Stabilization of the amplitude of alternans PDE under optimal full-state feedback control with LR1 model parameters. . . . .	19
2.5	Stabilization of the amplitude of alternans PDE under optimal full-state feedback control with Fox model parameters. . . . .	20
2.6	Stabilization of the amplitude of calcium alternans PDE under optimal full-state feedback control with Fox model parameters. . . . .	21
2.7	Trajectories of boundary input $v(t)$ for the LR1 and Fox ionic models under optimal full-state feedback control. . . . .	21
2.8	Trajectories of input derivative $\tilde{v}(t)$ for the LR1 and Fox ionic models under optimal full-state feedback control. . . . .	22
2.9	Trajectory of $u_{Ca}(t)$ for the Fox ionic model under optimal full-state feedback control. . . . .	22
3.1	Eigenspectrum of $\mathcal{A}^e$ for different cable lengths . . . . .	33
3.2	Stabilization of the amplitude of alternans PDE with model predictive control . . . . .	35
3.3	Trajectory of $v(t)$ under model predictive control. Constraints are shown as red dotted lines. . . . .	35
3.4	Trajectory of $u_{Ca}(t)$ under model predictive control. Constraints are shown as red dotted lines . . . . .	36

3.5	Trajectory of $y(t)$ under model predictive control. Constraints are shown as red dotted lines. . . . .	36
4.1	Stabilization of the amplitude of alternans PDE under robust MPC. . . . .	46
4.2	Trajectory of the boundary input $v(t)$ . The red dotted line depicts the lower bound on $v(t)$ . . . . .	46
4.3	Trajectory of $u_{Ca}(t)$ . Constraints are shown as red dotted lines . . . . .	47
4.4	Trajectory of $y(t)$ , which is $a(\zeta, t)$ measured at $\zeta_c = 4.125$ cm. The upper bound on $y(t)$ is shown as a red dotted line. . . . .	47

# Chapter 1

## Introduction

### 1.1 Motivation

Sudden cardiac death (SCD) is a leading cause of death in the United States, claiming over 350,000 lives annually [1]. Specifically, ventricular fibrillation (VF), which is a type of heart rhythm disorder known as arrhythmia, has been identified as the primary reason behind the majority of fatal cardiac arrests [2,3]. Multiple studies [4–6] have identified cardiac alternans as a possible precursor to VF. Alternans are defined as the beat-to-beat alternation in the action potential duration (APD). On an electrocardiogram (ECG), these alternans appear as alternations in the T-wave segments. Clinical studies have shown that the presence of T-wave alternans, even in small amounts, increases the risks of VF [4, 7].

Alternations in the APD can be induced in the cardiac tissue by applying a rapid pacing protocol. Associated with each action potential is a resting period known as the diastolic interval (DI). Reducing the pacing period shortens the DI, and as a result the tissue does not have enough time to fully recover before the next stimulus is applied, thus yielding a shorter APD. This leads to a period-doubling bifurcation, depicted by the black line in Fig. 1.1, where the following pattern emerges: short APD  $\rightarrow$  long DI  $\rightarrow$  long APD  $\rightarrow$  short DI. The mechanism linking T-wave alternans to the initiation of reentrant VF was studied in [4]. It was found that discordant alternans, which is the phenomenon where different regions of the tissue alternate out of phase with each other, are responsible for creating large spatial gradients (i.e. dispersion) of repolarization, which is an important condition for the development of reentrant arrhythmia. On the other hand, it was found that concordant alternans do not produce large enough spatial gradients of repolarization to cause VF. However, in the presence of heterogeneities of repolarization properties between the cardiac cells, concordant alternans may transform into discordant alternans.

The effect of electrical wave propagation instabilities caused by alternans is more evident in two (or higher) dimensional cardiac tissues, where simulation studies have shown that the presence

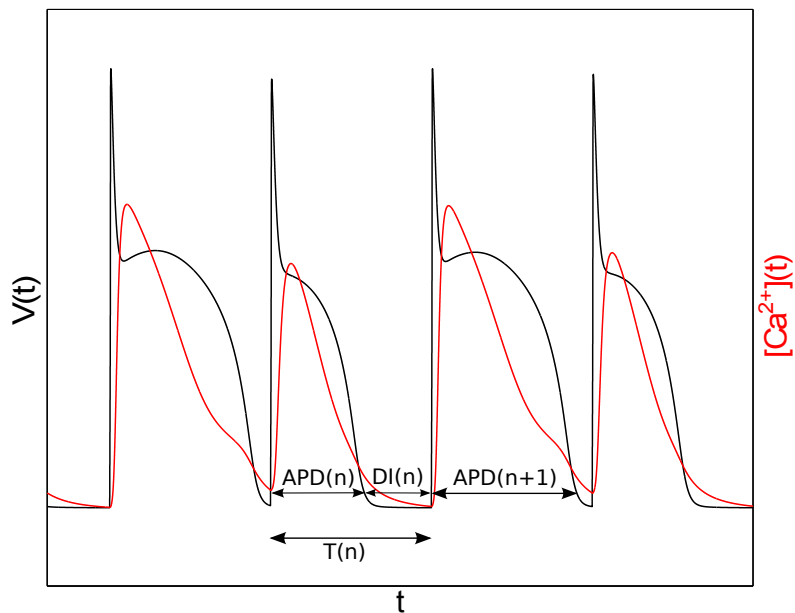


Figure 1.1: Time evolution of transmembrane potential (black) and intracellular calcium concentration (red) in the presence of alternans. APD and DI correspond to systolic (high) and diastolic (low) blood pressures.

of large oscillations in the APD can lead to spiral wave breakup and wave turbulence [8, 9]. A local wave break is caused by propagation failure (conduction block) which happens when the DI following a long APD falls below the threshold value required for the propagation of the next wave. This break will then initiate new spirals, which may also break by a similar mechanism.

Having established a causal link between alternans and VF (and consequently SCD), it is believed that the annihilation of these spatiotemporal alternans can serve as a promising anti-arrhythmic strategy.

## 1.2 Background

Cardiac cells are excitable cells, in which the transmembrane potential goes through a large excursion, called an action potential, when a large enough electrical stimulus is applied to the cell [10]. The cell membrane contains protein channels and carriers, which facilitate the flow of ions across the membrane. This ionic transport process is critical for the regulation of the cell's intracellular ionic composition. The membrane is selectively permeable, meaning that it will allow certain ions to diffuse through it but not others. Additionally, the membrane is more permeable to certain ionic species than to others. As a result, the movement of certain ions through the membrane can create a charge imbalance, which in turn sets up an electric field. An equilibrium is reached when this

electric field exactly balances the diffusion of the ionic species. At equilibrium, the potential difference across the membrane, which is dependent on the intra- and extra-cellular concentrations of the ionic species, is known as the Nernst potential  $V_S$  [10]. By convention, the transmembrane potential across the membrane,  $V$ , is defined as the difference between the intracellular and extracellular potentials. When  $V = V_S$ , there is no net current of the ionic species. When the cell is electrically stimulated, the movement of ions across the cell membrane results in an action potential.

A 1D cable of cardiac cells can be modeled as an excitable medium, and the propagation of action potentials along the cable is described by the following cable equation:

$$\frac{\partial V(\zeta, t)}{\partial t} = D \frac{\partial^2 V(\zeta, t)}{\partial \zeta^2} - \frac{I_{ion}(\zeta, t)}{C_m} \quad (1.1)$$

with boundary conditions:

$$\frac{\partial V(0, t)}{\partial \zeta} = V_p(t) \quad \frac{\partial V(L, t)}{\partial \zeta} = 0 \quad (1.2)$$

The first term on the right hand side of (1.1) describes the propagation of action potentials from one cell to another due to the diffusive coupling between the cells.  $V_p(t) = I_{stim}/C_m$  is the electrical stimulus applied at one end of the cable. Finally,  $D = 0.001 \text{ cm}^2/\text{ms}$  and  $C_m = 1 \text{ } \mu\text{F}/\text{cm}^2$  are the diffusivity constant and the cell membrane capacitance, respectively.  $I_{ion}(\zeta, t)$  represents the sum of the ionic currents that pass through the cell membrane during an action potential. Various models are available for  $I_{ion}(\zeta, t)$ , with varying degrees of accuracy and complexity. For most of these models, known as ionic models, the main ionic species that contribute to the overall ionic current are  $\text{Na}^+$ ,  $\text{K}^+$  and  $\text{Ca}^{2+}$ .

During an action potential propagation, the transmembrane potential and the intracellular  $[\text{Ca}^{2+}]$  transient are bidirectionally coupled [11–13]. In the case of positive  $V \rightarrow \text{Ca}^{2+}$  coupling, a longer APD corresponds to a higher peak  $\text{Ca}^{2+}$  transient, and vice versa. Similarly, for positive  $\text{Ca}^{2+} \rightarrow V$  coupling, a larger  $\text{Ca}^{2+}$  release will prolong the APD, and vice versa. In this work, we only consider the case when both couplings are positive, as shown in Figure 1.1, which leads to concordant (spatially synchronized) alternans [12].

### 1.2.1 The control problem

Most of the existing alternans annihilation methods are solely based on modulating the pacing interval at the tissue boundary. The pacing interval is modulated based on measurements of consecutive APDs at the pacing site. This electrical boundary control strategy has been shown to be effective in small tissues [4, 14–16]. However, it has been shown analytically and experimentally that this control strategy has a finite degree of controllability, such that alternans stabilization in cardiac tissues  $> 1 \text{ cm}$  cannot be achieved [4, 14–20]. One reason for this limitation is the fact

that the feedback law is based on only one measurement site and therefore does not account for the spatially distributed nature of the tissue’s electrical dynamics. Furthermore, since this control strategy is non-model based, there is an inherent limitation on the controller gain in order to prevent conduction block. As demonstrated by [21], for alternans suppression in a ring geometry, a model-based LQR (Linear Quadratic Regulator) control scheme significantly outperforms the non-model-based control scheme. The same conclusion was reached in [22] for the open fiber (the Purkinje fiber). However, as demonstrated in [22], the optimal model-based control algorithm is only successful up to  $L \approx 2$  cm. Recently, it has been shown that oscillations in the pacing cycle length can induce alternans in the heart [23]. A stochastic pacing protocol that annihilates alternans by reducing the slope of the APD resitution curve was then developed by [24]. However, this study was limited to small cardiac tissues (1 cm x 1 cm).

The intracellular calcium cycle is shown in Figure. 1.2 [25]. This dynamics plays a critical role in the mechanical contraction and relaxation of the cardiac muscle. For instance, the binding of  $\text{Ca}^{2+}$  to Troponin C leads to the generation of active stress in the sarcomere [26]. Therefore, this coupling between the transmembrane potential and the  $\text{Ca}^{2+}$  dynamics leads to the electromechanical coupling in cardiac tissues, in which mechanically induced stretching of the tissue affects its electrical activity, and vice versa [27–29]. Specifically, [30] has demonstrated that an axial stretch in the direction of the fibers will prolong the APD. This electromechanical coupling provides the motivation for including a  $\text{Ca}^{2+}$ -based actuator to our control strategy. By modulating the intracellular  $\text{Ca}^{2+}$  concentration, the tissue’s mechanical properties are altered, thus affecting the APD. Through the inclusion of this second actuator, which is completely independent of the boundary electrical pacing, we believe that the controllability limitation pointed out in [19, 20, 22] can be overcome.

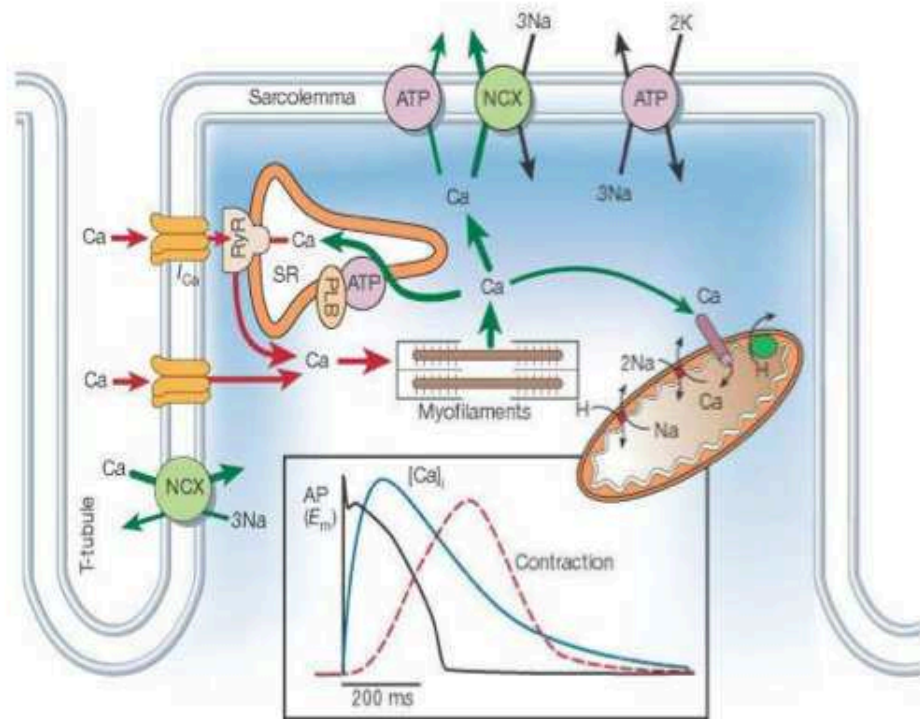


Figure 1.2: Intracellular  $[Ca^{2+}]$  dynamics

### 1.3 Thesis outline and contributions

In this thesis, the annihilation of cardiac alternans is demonstrated through the application of three different model based control strategies. The system to be controlled is given in the form of a parabolic partial differential equation (PDE) which describes the spatiotemporal dynamics of the small amplitude of APD alternans [31]. In Chapter 2, an additional PDE that describes the spatiotemporal dynamics of the peak intracellular  $[Ca^{2+}]$  is also studied [12]. The spatial operator of each PDE has an eigenspectrum that can be partitioned into a finite-dimensional slow (unstable) component and an infinite dimensional fast (stable) component. This property allows for the formulation of a low order controller that is able to stabilize the entire system [32, 33]. In all three controller formulations, the control inputs include one boundary actuation and a spatially distributed,  $Ca^{2+}$ -based actuator.

In Chapter 2, an optimal full state feedback control strategy is developed for the system of two PDEs. Two cases are considered: one in which the coupling is unidirectional, and another where the coupling is bidirectional. The effect of coupling on the controller performance is discussed.

In Chapter 3, a constrained model predictive controller (MPC) is developed for the amplitude of APD alternans PDE. The MPC framework is suitable for this application, since constraints can

be handled explicitly in the controller formulation. In working with the cardiac system, certain constraints must not be violated in order to ensure that the control action will not induce conduction block. Additional constraints may also be present for the actuators.

The issue of model uncertainty is addressed in Chapter 4, where an LMI (Linear Matrix Inequality)-based, constrained robust MPC is developed for the amplitude of APD alternans PDE. In this formulation, the class of uncertain models arise from the uncertainties in the PDE parameters. This approach ensures that the resulting controller can achieve closed loop stability for the specified range of model uncertainties.

Finally, concluding remarks and future research direction are presented in Chapter 5.

## Chapter 2

# Optimal control of cardiac alternans

### 2.1 Introduction

In this chapter, we propose an optimal full state feedback control strategy for the annihilation of cardiac alternans in a 1D cable of cardiac cells, using a combination of boundary and spatially distributed,  $\text{Ca}^{2+}$ -based actuation. The controller is formulated based on a system of two parabolic PDEs. The first PDE describes the spatiotemporal dynamics of the amplitude of APD alternans [31], while the second PDE describes the spatiotemporal dynamics of the peak intracellular  $[\text{Ca}^{2+}]$  [12]. This model formulation takes into account the coupling between APD and the cardiac cell's intracellular  $\text{Ca}^{2+}$  concentration.

A similar optimal control strategy was previously developed by [34]. However, in [34], the authors did not account for the spatial evolution of the  $[\text{Ca}^{2+}]$  transient along the cable of cardiac cells. In this work, the control strategy is applied to the system of coupled PDEs, such that the cardiac system's calcium dynamics is relevantly represented. These PDEs belong to a class of parabolic PDEs that describe diffusion-convection-reaction processes. By transforming the system of PDEs into an abstract evolutionary form and partitioning its spectrum into slow (finite dimensional) and fast (infinite dimensional) subsystems, the finite-dimensional optimal state feedback controller can be obtained, as presented in [32,33]. In this method, the boundary actuator, which represents a pacing algorithm, is applied at one end of the cable, while the calcium-based actuator is applied over a specific region of the cable. This calcium-based actuator modulates the intracellular  $\text{Ca}^{2+}$  concentration and can be realized using a drug that affects the calcium channels in the cardiac cells (tissue), delivered using either a patch or an implantable device.

The main contribution of the research efforts demonstrated in this work is to extend the understanding and to provide a theoretical analysis for the novel idea of a combined pacing and mechano-electric ( $\text{Ca}^{2+}$ )-based alternans annihilation in a relevantly sized cardiac cable. The dynamical analysis of spatiotemporal voltage and calcium coupling arising from relevant ionic models

(LR1, Fox, etc.) and model based control synthesis provide a foundation to seek alternans annihilation realizations in the cardiac cable of size greater than 1 cm.

This chapter is organized as follows. Section 2.2 introduces the amplitude of alternans PDEs and the system's state space representation. The optimal controller formulation is presented in Section 2.3, and numerical simulation results are given in Section 2.4. To conclude the chapter, a brief summary is provided in Section 2.5.

## 2.2 Model description

### Amplitude equations

The amplitude of alternans,  $a(\zeta, n)$ , is defined as the difference between two consecutive APDs. That is,

$$a(\zeta, n) = (\text{APD}_{\zeta, n} - \text{APD}_{\zeta, n-1})(-1)^n \quad (2.1)$$

Using the fact that close to the critical pacing rate,  $a(\zeta, n)$  varies slowly from beat to beat, Echebarria and Karma [31] derived the PDE that describes the spatiotemporal dynamics of the small amplitude of alternans. Similarly, based on [12], a PDE describing the spatiotemporal dynamics of the peak intracellular  $[\text{Ca}^{2+}]$ , denoted as  $a_{Ca}(\zeta, t)$ , can be written. For a 1D cable, the system of PDEs is given by:

$$\frac{\partial a(\zeta, t)}{\partial t} = \text{Da}_1 \frac{\partial^2 a(\zeta, t)}{\partial \zeta^2} - \omega_1 \frac{\partial a(\zeta, t)}{\partial \zeta} + \sigma a(\zeta, t) - ga(\zeta, t)^3 + \eta a_{Ca}(\zeta, t) \quad (2.2a)$$

$$\frac{\partial a_{Ca}(\zeta, t)}{\partial t} = \text{Da}_2 \frac{\partial^2 a_{Ca}(\zeta, t)}{\partial \zeta^2} - \omega_2 \frac{\partial a_{Ca}(\zeta, t)}{\partial \zeta} + \gamma a(\zeta, t) + \sum_{i=1}^m b_{Ca, i}(\zeta) u_{Ca, i}(t) \quad (2.2b)$$

With boundary conditions

$$\frac{\partial a(0, t)}{\partial \zeta} = a(0, t) + v(t) \quad \frac{\partial a(L, t)}{\partial \zeta} = 0 \quad (2.2c)$$

$$\frac{\partial a_{Ca}(0, t)}{\partial \zeta} = a_{Ca}(0, t) \quad \frac{\partial a_{Ca}(L, t)}{\partial \zeta} = 0 \quad (2.2d)$$

All the PDE parameters are normalized with respect to  $\tau$ , the pacing period. In Eqs. 2.2a and 2.2b, the parameters  $\text{Da}_i$  and  $\omega_i$  describe the propagation of the amplitudes by diffusion and convection, respectively. Although there is no diffusion of  $\text{Ca}^{2+}$  between the adjacent cells, we expect that the alternations in  $a_{Ca}(\zeta, t)$  will propagate along the cable in a similar fashion to that of  $a(\zeta, t)$  due to the bidirectional coupling between them. Therefore, it is assumed that  $\text{Da}_1 = \text{Da}_2 = \text{Da}$  and  $\omega_1 = \omega_2 = \omega$ . The term  $\sigma a(\zeta, t)$  represents the growth of the amplitude of alternans along the cable, while the term  $ga(\zeta, t)^3$  ensures that the evolution of  $a(\zeta, t)$  is bounded. In this work, we assume that alternans arise from the instabilities in the voltage dynamics and not the  $[\text{Ca}^{2+}]$  dynamics.

Therefore, these two terms are omitted in Eq. 2.2b. Finally  $\eta$  and  $\gamma$  are the coupling parameters that relate the two PDEs.

The boundary actuation, which represents a pacing protocol applied at  $\zeta = 0$ , is denoted by  $v(t)$ , while the spatially distributed actuation is denoted by  $u_{Ca}(t)$ . This calcium-based actuation acts directly on the  $a_{Ca}(\zeta, t)$  system in order to suppress the alternations in the intracellular  $\text{Ca}^{2+}$  concentration, but also helps in stabilizing the  $a(\zeta, t)$  system through the coupling between the two PDEs. The placement of the  $i^{\text{th}}$  calcium-based actuator on the cable is described by the function  $b_{Ca,i}(\zeta)$ , and the summation term in Eq. 2.2b represents the overall effect of the calcium-based actuator(s) on the system.

The parameters  $\text{Da}$ ,  $\omega$ ,  $\sigma$  and  $g$  are obtained from the restitution curve, which describes the relationship between the  $(n+1)^{\text{th}}$  APD and the previous DI, i.e.  $\text{APD}^{n+1} = f(\text{DI}^n)$ . The restitution curve for the Fox ionic model is shown in Figure 2.1. This figure was obtained by applying the S1S2 pacing protocol to a single cardiac cell. In this protocol, the cell is initially paced at a sufficiently large pacing cycle length ( $\text{PCL}_{S1}$ ) for fifty beats, followed by a shorter cycle length ( $\text{PCL}_{S2}$ ). This is repeated for decreasing values of  $\text{PCL}_{S2}$ , until conduction block is induced. The electrical stimulus is applied as square wave pulses with a magnitude of  $80 \mu\text{A}/\mu\text{F}$  and a duration of 1 ms [35]. The APD was measured as APD90, which is the APD at 90% repolarization.

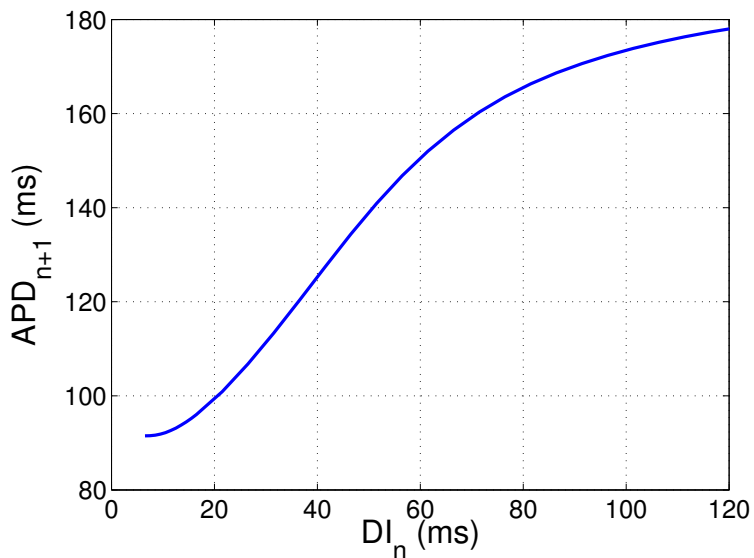


Figure 2.1: Restitution curve for the Fox ionic model obtained using an S1 period of 350 ms and S2 periods ranging from 340 to 200 ms.

For the PDE parameters, two ionic models are considered, namely the Luo-Rudy (LR1) model given in [36] and the Fox model presented in [35]. The main difference between these two ionic models lies in the treatment of the intracellular  $[\text{Ca}^{2+}]$  dynamics. The Fox ionic model explicitly

accounts for the bidirectional coupling between the transmembrane potential and the intracellular  $\text{Ca}^{2+}$  concentration, while the LR1 model does not.

Based on [31], the PDE parameters are defined as:  $\text{Da} \approx D \times \text{APD}_c$ ,  $\omega \approx 2D/c$ ,  $\sigma \approx \log(f')$  and  $g \approx (f'')^2/4 - f'''/6$ , with all derivatives computed at the bifurcation point, defined as the pacing period at which persistent alternans start to emerge.  $\text{APD}_c$  is the APD at the bifurcation point, and  $c$  is the wave propagation speed computed at the bifurcation point. Refer to [31] for the detailed derivation and physical interpretation of these parameters. To identify  $\gamma$ , the S1S2 pacing protocol described previously is again applied to the single cell, and the peak  $\text{Ca}^{2+}$  concentration at S2 is plotted against the DI at S1.  $\gamma$  is then obtained by computing the slope of this curve at the bifurcation point. The identification of  $\eta$  is performed by pacing the single cell at a period close to the the bifurcation point for approximately 50 beats, and then introducing an external  $[\text{Ca}^{2+}]$  signature (obtained from a separate simulation with a different pacing period) for the following beat.  $\eta$  is then approximated by the ratio  $\frac{\Delta a}{\Delta a_{\text{Ca}}}$ . Note that since the LR1 model does not account for the coupling between  $a_{\text{Ca}}(\zeta, t)$  and the transmembrane potential,  $\eta$  for this model is set to zero.

### 2.2.1 State space system representation

For the following procedure, the PDEs given by Eq. 2.2 are first linearized around their spatially uniform unstable steady states ( $a(\zeta, t) = 0$  and  $a_{\text{Ca}}(\zeta, t) = 0$ ). Eqs. 2.2a and 2.2c can then be formulated as the following abstract boundary control problem:

$$\begin{aligned} \frac{da(t)}{dt} &= \mathcal{F}a(t) + \eta a_{\text{Ca}}(t) & t \geq 0 \\ a(0) &= a_0 \\ \mathcal{B}a(t) &= v(t) \end{aligned} \tag{2.3}$$

Where  $a(\cdot, t) = \{a(\zeta, t), 0 \leq \zeta \leq L\}$  and  $a_{\text{Ca}}(\cdot, t) = \{a_{\text{Ca}}(\zeta, t), 0 \leq \zeta \leq L\}$  are state variables in the Hilbert space  $\mathcal{L}_2([0, L]; t)$  [32],  $t$  is the time variable and  $v(t) \in \mathbb{R}$  is the boundary actuation.  $\mathcal{F}$  is the spatial derivative operator defined as:

$$\mathcal{F}\phi(\zeta) = \left[ \text{Da} \frac{d^2}{d\zeta^2} - w \frac{d}{d\zeta} + \sigma \right] \phi(\zeta) \tag{2.4}$$

with the domain  $\mathcal{D}(\mathcal{F}) = \{\phi(\zeta) \in L_2(0, L) : \phi(\zeta), \phi'(\zeta) \text{ are abs. cont.}, \mathcal{F}\phi(\zeta) \in L_2(0, L), \text{ and } \phi'(L) = 0\}$ . Here  $L_2(0, L)$  denotes the Hilbert space of measurable, square-integrable, real-valued functions with weighted inner product and norm defined as  $\langle f, g \rangle_{\mu, L_2} = \int_0^L e^{-\mu\zeta} f(\zeta)g(\zeta)d\zeta$ , and  $\|f\|_2 =$

$\sqrt{\langle f, f \rangle_{\mu, L_2}}$ , respectively. The boundary operator  $\mathcal{B} : L_2(0, L) \mapsto \mathbb{R}$  can be defined as follows:

$$\mathcal{B}\phi(\zeta) = \frac{\delta\phi(0)}{\delta\zeta} - \phi(0), \text{ with } \mathcal{D}(\mathcal{F}) \subset \mathcal{D}(\mathcal{B}) \quad (2.5)$$

Eq. 2.3 is not well posed, due to the fact that the controlled input appears in the boundary condition. Therefore, we define a new operator  $\mathcal{A}_1$  such that

$$\mathcal{A}_1\phi(\zeta) = \mathcal{F}\phi(\zeta), \text{ and } \mathcal{D}(\mathcal{A}_1) = \mathcal{D}(\mathcal{F}) \cup \ker(\mathcal{B}) \quad (2.6)$$

This is based on the assumption that  $v(t) \in \mathbf{C}^2([0, t]; V)$  is sufficiently smooth, and one can find a function  $B(\zeta)$  such that  $\forall v(t), B(\zeta)v(t) \in \mathcal{D}(\mathcal{F})$ , and

$$\mathcal{B}B(\zeta)v(t) = v(t), \quad v(t) \in V \quad (2.7)$$

Furthermore, without loss of generality, we can choose  $B(\zeta)$  such that  $\mathcal{F}B(\zeta) = 0$ . Knowing  $B(\zeta)$ , we define the following state transformation:

$$a(\zeta, t) = p(\zeta, t) + B(\zeta)v(t) \quad (2.8)$$

Substituting Eq. 2.8 into Eq. 2.3, we obtain the following well posed abstract differential equation:

$$\begin{aligned} \frac{\partial p(\zeta, t)}{\partial t} &= \mathcal{A}_1 p(\zeta, t) + \mathcal{F}B(\zeta)v(t) + \eta a_{Ca}(\zeta, t) - B(\zeta)\dot{v}(t) \quad t \geq 0 \\ p(\zeta, 0) &= p_0(\zeta) \end{aligned} \quad (2.9)$$

Interestingly, in Eq. 2.9, the boundary actuation is manifested as a time derivative when it is transferred into the domain of the PDE setting. This can be seen as a constraint on the pacing protocol, since  $\dot{v}(t)$  needs to be a sufficiently smooth function. Additionally, it is important to note that the transformation given by Eq. 2.8 must be exact to ensure that any noise at the boundary will not be amplified throughout the system.

A similar abstract evolutionary form can be formulated for the  $a_{Ca}(\zeta, t)$  PDE:

$$\begin{aligned} \frac{da_{Ca}(t)}{dt} &= \gamma a(t) + \mathcal{A}_2 a_{Ca}(t) + \mathcal{B}_{Ca} u_{Ca}(t) \quad t \geq 0 \\ a_{Ca}(0) &= a_{Ca_0} \end{aligned} \quad (2.10)$$

Where the spatial derivative operator  $\mathcal{A}_2$  is given by:

$$\mathcal{A}_2\psi(\zeta) = \left[ \text{Da} \frac{d^2}{d\zeta^2} - w \frac{d}{d\zeta} \right] \psi(\zeta) \quad (2.11)$$

with the domain  $\mathcal{D}(\mathcal{A}_2) = \{\psi(\zeta) \in L_2(0, L) : \psi(\zeta), \psi'(\zeta) \text{ are abs. cont.}, \mathcal{A}_2\psi(\zeta) \in L_2(0, L), \psi'(0) - \psi(0) = 0, \text{ and } \psi'(L) = 0\}$ . For the spatially distributed actuators, we define:

$$\mathcal{B}_{Ca} u_{Ca}(t) = \sum_{i=1}^m b_{Ca,i}(\zeta) u_{Ca,i}(t), \quad (2.12)$$

where  $b_{Ca,i}(\zeta) = \frac{1}{2\epsilon}$  for  $\zeta \in [\zeta_i - \epsilon, \zeta_i + \epsilon]$ ,  $\epsilon > 0$  is a function describing the locations of the actuators. Here, we only consider one spatially distributed actuator and the index  $i$  will be dropped.

Combining Eqs. 2.9 and 2.10, and defining  $v(t)$  as a new state variable, the PDE system given by Eqs. 2.2a - 2.2d is reformulated on the extended state space  $\mathcal{L}_2^e := \mathcal{L}_2 \otimes V$ , yielding

$$\begin{aligned} \dot{x}(\zeta, t) &= \begin{bmatrix} 0 & 0 & 0 \\ \mathcal{F}B & \mathcal{A}_1 & \eta \\ \gamma B & \gamma & \mathcal{A}_2 \end{bmatrix} \begin{bmatrix} v(t) \\ p(\zeta, t) \\ a_{Ca}(\zeta, t) \end{bmatrix} + \begin{bmatrix} 1 & 0 \\ -B & 0 \\ 0 & \mathcal{B}_{Ca} \end{bmatrix} \begin{bmatrix} \tilde{v}(t) \\ u_{Ca}(t) \end{bmatrix} \\ &= \mathcal{A}^e x(\zeta, t) + \mathcal{B}^e u(t) \\ x(\zeta, 0) &= \begin{bmatrix} v(0) & p(\zeta, 0) & a_{Ca}(\zeta, 0) \end{bmatrix}' = x_0(\zeta) \end{aligned} \quad (2.13)$$

Here,  $\tilde{v}(t) = \dot{v}(t)$ . Physiologically,  $\tilde{v}(t)$  can be interpreted as the rate of change of pacing period applied at the boundary.

### The eigenvalue problem

By solving the eigenvalue problem  $\mathcal{A}\phi(\zeta) = \lambda\phi(\zeta)$ , the eigenvalues and corresponding eigenfunctions of  $\mathcal{A}_1$  and  $\mathcal{A}_2$  can be found analytically through the separation of variables [32]. Furthermore, eigenfunctions of the adjoint operators  $\mathcal{A}_1^*$  and  $\mathcal{A}_2^*$  that satisfy the orthogonality condition  $\langle \phi_i(\zeta), \phi_j^*(\zeta) \rangle = \delta_{ij}$  can also be computed. The eigenvalues for  $\mathcal{A}_1$  and  $\mathcal{A}_2$  are respectively given by:

$$\lambda_i = \sigma - \text{Da} \left[ \alpha_i + \frac{\omega^2}{4\text{Da}^2} \right], \quad 0 < \alpha_i < \alpha_{i+1}, \quad i \geq 1 \quad (2.14a)$$

$$\bar{\lambda}_i = -\text{Da} \left[ \alpha_i + \frac{\omega^2}{4\text{Da}^2} \right], \quad 0 < \alpha_i < \alpha_{i+1}, \quad i \geq 1, \quad (2.14b)$$

where  $\alpha_i$  are the solutions to the following transcendental equation:

$$\tan(\sqrt{\alpha_i}L) = \frac{\sqrt{\alpha_i}}{\alpha_i - \frac{\omega}{2\text{Da}} \left(1 - \frac{\omega}{2\text{Da}}\right)} \quad (2.15)$$

In Eq. 2.13, the spatial derivative operators  $\mathcal{A}_1$  and  $\mathcal{A}_2$  are Sturm-Liouville operators which can be written in the following form:

$$\mathcal{A}\phi(\cdot) = \frac{1}{\rho(\cdot)} \frac{d}{d\zeta} \left[ p(\cdot) \frac{d\phi}{d\zeta}(\cdot) \right] + q(\cdot)\phi(\cdot) \quad (2.16)$$

Comparing the coefficients of Eq. 2.16 with those of Eqs. 2.4 and 2.11, we obtain  $\rho(\zeta) := \exp^{-\frac{\omega}{\text{Da}}\zeta}$ ,  $p(\zeta) := \text{Da}\rho(\zeta)$ ,  $q(\zeta) := \sigma$  for  $\mathcal{A}_1$  and  $q(\zeta) = 0$  for  $\mathcal{A}_2$ . For  $\mathcal{A}_1$ , the eigenfunctions and adjoint eigenfunctions for  $i \geq 1$  are given by:

$$\phi_i(\zeta) = B_i \exp^{\frac{\omega}{2\text{Da}}\zeta} \left[ \cos(\sqrt{\alpha_i}\zeta) + \frac{1}{\sqrt{\alpha_i}} \left(1 - \frac{\omega}{2\text{Da}}\right) \sin(\sqrt{\alpha_i}\zeta) \right] \quad (2.17a)$$

$$\phi_i^*(\zeta) = \exp^{-\frac{\omega}{\text{Da}}\zeta} \phi_i(\zeta) \quad (2.17b)$$

The coefficients  $B_i$ 's are obtained by imposing the orthogonality condition  $\langle \phi_i(\zeta), \phi_j^*(\zeta) \rangle = \delta_{ij}$ , and are evaluated as:

$$B_i = \left\{ \int_0^L \left[ \cos(\sqrt{\alpha_i}\zeta) + \frac{1}{\sqrt{\alpha_i}} \left(1 - \frac{\omega}{2\text{Da}}\right) \sin(\sqrt{\alpha_i}\zeta) \right]^2 d\zeta \right\}^{-1/2} \quad (2.18)$$

For  $\mathcal{A}_2$ , the eigenfunctions and adjoint eigenfunctions are equal to those of  $\mathcal{A}_1$ . This is because the PDE parameters in Eqs. 2.2a and 2.2b are equal except for the growth term  $\sigma$ , and the eigenfunctions are independent of this term. Thus,

$$\psi_i(\zeta) = \phi_i(\zeta), \text{ and } \psi_i^*(\zeta) = \phi_i^*(\zeta) \quad (2.19)$$

In general, the eigenvalues and eigenfunctions of  $\mathcal{A}^e$  cannot be determined analytically. However, in the special case where  $\eta = 0$  (i.e. the LR1 case),  $\mathcal{A}^e$  has a lower triangular structure. In this case, the eigenvalue problem for this extended operator can be solved analytically. First, note that  $\mathcal{A}^e$  can be written as:

$$\mathcal{A}^e = \begin{bmatrix} 0 & 0 \\ A_3 & \mathcal{A} \end{bmatrix}, \text{ with } \mathcal{A} = \begin{bmatrix} \mathcal{A}_1 & 0 \\ \gamma & \mathcal{A}_2 \end{bmatrix} \text{ and } A_3 = \begin{bmatrix} \mathcal{F}B \\ B \end{bmatrix}.$$

Since  $\mathcal{A}$  is a lower triangular matrix, its eigenspectrum is given by  $\Omega(\mathcal{A}) = \Omega(\mathcal{A}_1) \cup \Omega(\mathcal{A}_2)$ . That is,

$$\Omega(\mathcal{A}) = \Lambda_j = \begin{cases} \lambda_i & \text{when } j \text{ is odd} \\ \bar{\lambda}_i & \text{when } j \text{ is even} \end{cases} \quad (2.20)$$

Denoting the eigenfunctions of  $\mathcal{A}$  as  $\Phi_j(\zeta) = [\xi_{1,j} \quad \xi_{2,j}]'$ , we have

$$\begin{bmatrix} \mathcal{A}_1 & 0 \\ \gamma & \mathcal{A}_2 \end{bmatrix} \begin{bmatrix} \xi_{1,j} \\ \xi_{2,j} \end{bmatrix} = \Lambda_j \begin{bmatrix} \xi_{1,j} \\ \xi_{2,j} \end{bmatrix} \quad (2.21)$$

Eq. 2.21 leads to a system of two algebraic equations for each  $\Lambda_j$ . Solving these equations, and utilizing the definition of resolvent sets [32], we obtain the following expression:

$$\Phi_j(\zeta) = \begin{cases} \begin{bmatrix} \phi_i(\zeta) & \frac{\gamma}{\sigma} \psi_i(\zeta) \end{bmatrix}' & \text{when } j \text{ is odd} \\ \begin{bmatrix} 0 & \psi_i(\zeta) \end{bmatrix}' & \text{when } j \text{ is even} \end{cases} \quad (2.22)$$

The eigenfunctions of the adjoint operator  $\mathcal{A}^*$  can be found using the same procedure. These are given by:

$$\Psi_j(\zeta) = \begin{cases} \begin{bmatrix} \phi_i^*(\zeta) & 0 \end{bmatrix}' & \text{when } j \text{ is odd} \\ \begin{bmatrix} -\frac{\gamma}{\sigma} \phi_i^*(\zeta) & \psi_i^*(\zeta) \end{bmatrix}' & \text{when } j \text{ is even} \end{cases} \quad (2.23)$$

The same procedure is again repeated for the extended spatial operator  $\mathcal{A}^e$ , whose eigenspectrum is given by  $\Omega(\mathcal{A}^e) = \{0\} \cup \Omega(\mathcal{A}) = \{0\} \cup \{\lambda_i\} \cup \{\bar{\lambda}_i\}$ . If there are  $m$  boundary input variables, the zero

eigenvalue will be repeated  $m$  times. Here,  $m = 1$ . The eigenfunction and adjoint eigenfunction corresponding to the zero eigenvalue are given by:

$$\hat{\Phi}_0(\zeta) = \begin{bmatrix} 1 \\ \sum_{j=1}^{\infty} \frac{1}{\Lambda_j} \langle A_3(\zeta), \Psi_j(\zeta) \rangle \Phi_j(\zeta) \end{bmatrix} \text{ and } \hat{\Psi}_0(\zeta) = \begin{bmatrix} 1 \\ 0 \end{bmatrix} \quad (2.24)$$

while those corresponding to the remaining eigenvalues are given by:

$$\hat{\Phi}_j(\zeta) = \begin{bmatrix} 0 \\ \Phi_j(\zeta) \end{bmatrix} \text{ and } \hat{\Psi}_j(\zeta) = \begin{bmatrix} \frac{1}{\Lambda_j} A_3^*(\zeta) \Psi_j(\zeta) \\ \Psi_j(\zeta) \end{bmatrix} \quad (2.25)$$

### Modal decomposition

Parabolic systems such as Eq. 2.2 can be realized through modal decomposition. In the case where the PDE parameters are obtained from the LR1 model, the decomposition can be performed directly on the extended state  $x(\zeta, t)$ , since the eigenfunctions of  $\mathcal{A}^e$  can be found analytically, as given by Eqs. 2.24 and 2.25. By substituting  $x(\zeta, t) = \sum_{j=1}^{\infty} c_j(t) \hat{\Phi}_j(\zeta)$  into Eq. 2.13 and projecting the resulting system onto  $\hat{\Psi}_j(\zeta)$ , we obtain the following infinite-dimensional state space system:

$$\dot{c}(t) = \Lambda c(t) + \langle \mathcal{B}^e, \hat{\Psi}(\zeta) \rangle u(t) \quad (2.26)$$

where  $\Lambda$  is a diagonal matrix whose entries are the eigenvalues of  $\mathcal{A}^e$ .

On the other hand, when the PDE parameters are obtained using the Fox model, analytical expressions for  $\hat{\Phi}_j(\zeta)$  and  $\hat{\Psi}_j(\zeta)$  are not available. Therefore, each state variable must be decomposed separately, namely  $p(\zeta, t) = \sum_{i=1}^{\infty} p_i(t) \phi_i(\zeta)$  and  $a_{Ca}(\zeta, t) = \sum_{i=1}^{\infty} a_{Ca_i}(t) \psi_i(\zeta)$ . After applying the state transformation Eq. 2.8 and substituting these eigenfunction expansions into Eq. 2.13, for all  $i \geq 1$  we obtain:

$$\begin{bmatrix} 1 & 0 & 0 \\ 0 & \phi_i(\zeta) & 0 \\ 0 & 0 & \psi_i(\zeta) \end{bmatrix} \dot{x}_i(t) = \mathcal{A}_i^e \begin{bmatrix} 1 & 0 & 0 \\ 0 & \phi_i(\zeta) & 0 \\ 0 & 0 & \psi_i(\zeta) \end{bmatrix} x_i(t) + \mathcal{B}^e u(t) \quad (2.27)$$

Projecting Eq. 2.27 onto  $\begin{bmatrix} 1 & 0 & 0 \\ 0 & \phi_i^*(\zeta) & 0 \\ 0 & 0 & \psi_i^*(\zeta) \end{bmatrix}$ , we obtain:

$$\begin{aligned} \dot{x}_i(t) &= \begin{bmatrix} 0 & 0 & 0 \\ \langle \mathcal{F}B(\zeta), \phi_i^*(\zeta) \rangle & \lambda_i & \eta \\ \langle B(\zeta), \psi_i^*(\zeta) \rangle & \gamma & \bar{\lambda}_i \end{bmatrix} x_i(t) + \begin{bmatrix} 1 & 0 \\ -\langle B(\zeta), \phi_i^*(\zeta) \rangle & 0 \\ 0 & \langle b_{Ca}(\zeta), \psi_i^*(\zeta) \rangle \end{bmatrix} \tilde{u}(t) \\ &= A^e x_i(t) + B^e u(t) \end{aligned} \quad (2.28)$$

In this case, the overall system's eigenvalues must be computed numerically. Nonetheless, it is still possible to diagonalize the state matrix  $A^e$  using its eigenvectors, since all the eigenvalues

are distinct. These eigenvalues are dependent on the coupling parameters  $\eta$  and  $\gamma$ . When  $\eta$  and  $\gamma$  have opposite signs, depending on their magnitudes, one can potentially obtain conjugate complex eigenvalues, which will result in oscillatory coupling among the APD and calcium alternans. However, further parametric investigation is required to determine whether or not this can be realistically achieved. In this study, both  $\eta$  and  $\gamma$  are positive, and all eigenvalues are real.

The stability of the extended system given by Eq. 2.13 is governed by the eigenvalues of  $\mathcal{A}^e$ , which are dependent on the eigenvalues of the individual PDEs, namely  $\lambda_i$  and  $\bar{\lambda}_i$ . From Eq. 2.14b, it is apparent that  $\forall i, \bar{\lambda}_i < 0$ . This implies that in the absence of coupling, Eq. 2.2b is inherently stable. For the LR1 case, the overall system's eigenvalues are simply a union of  $\lambda_i$  and  $\bar{\lambda}_i$  (see Eq. 2.20). Therefore, in this case, due to the master-slave relationship between voltage and calcium dynamics, instabilities in the extended system arise solely from the  $a(\zeta, t)$  (voltage) subsystem. On the other hand, for the Fox model, each of the overall system's eigenvalues depend simultaneously on both  $\lambda_i$  and  $\bar{\lambda}_i$ . As a result, due to the bidirectional coupling between voltage and calcium dynamics, both subsystems contribute to the instabilities in the extended system.

## 2.3 Optimal controller formulation

The operators of the parabolic system given by Eq. 2.2 are dissipative, and the structure of their eigenspectra is beneficial for the formulation of a simple gain-based optimal full-state feedback control law which stabilizes the unstable modes, while the stable modes remain invariant to this control law. The eigenspectrum of  $\mathcal{A}^e$  can be divided into a finite-dimensional unstable (slow) part and an infinite-dimensional stable (fast) part, i.e.  $\Omega(\mathcal{A}^e) = \Omega^+(\mathcal{A}^e) \cup \Omega^-(\mathcal{A}^e)$ . The finite-dimensional optimal controller will then be developed based only on the unstable subsystem.

The optimal controller gain is obtained by solving the following minimization problem over an infinite time horizon:

$$\begin{aligned} \min_u J(x(0); u) &= \int_0^{\infty} [x_s(t)' Q x_s + u(t)' R u(t)] dt \\ \text{s.t. } \dot{x}_s(t) &= A_s^e x_s(t) + B_s^e u(t) \end{aligned} \quad (2.29)$$

where  $x_s(t)$ ,  $\mathcal{A}_s^e$  and  $\mathcal{B}_s^e$  have dimensions corresponding to that of the slow (unstable) subsystem  $\Omega^+(\mathcal{A}^e)$ .  $Q \geq 0$  and  $R > 0$  are the diagonal penalty matrices for the state and input variables, respectively. Solving this LQR problem, the optimal control law is obtained as:

$$u_{opt}(t) = -K_{opt} x_s(t) = -R^{-1} B_s^{e'} P x_s(t) \quad (2.30)$$

where  $P$  is a symmetric, positive definite solution to the Algebraic Riccati Equation

$$0 = A_s^{e'} P + P A_s^e + Q - P B_s^e R^{-1} B_s^{e'} P \quad (2.31)$$

## 2.4 Numerical simulation

In this section, we consider the system of PDEs given by Eq. 2.2, with parameters  $Da$ ,  $\omega$ ,  $\sigma$  and  $g$  obtained from the LR1 ionic model [36] and the Fox ionic model [35]. These parameters, as well as the coupling parameters  $\eta$  and  $\gamma$  are presented in Table 2.1. The critical pacing periods for the LR1 model and the Fox model were found to be 311 ms and 215 ms, respectively. For the each set of parameters, the eigenspectra for the operators  $\mathcal{A}_1$  and  $\mathcal{A}_2$  are computed according to Eqs. 2.14 - 2.15. The eigenspectrum of  $\mathcal{A}^e$  can then be obtained from these individual eigenvalues. The distribution of the eigenspectrum depends on the cable length  $L$ . As can be seen from Figures 2.2 and 2.3, the number of unstable eigenvalues increases with increasing cable length. In these simulations, a cable length of 6.25 cm is considered. Both Figures 2.2 and 2.3 show that for all cable lengths, there is a zero eigenvalue. This is because for both models,  $\Omega(\mathcal{A}^e) = \{0\} \cup \Omega(\mathcal{A})$ , where the zero eigenvalue arises from the presence of boundary actuation. This is a dynamical feature that has not been recognized in previous works, and implies that the system is effectively controlled by the time derivative of the boundary input and not the input itself.

Table 2.1: PDE parameter values for the LR1 and Fox ionic models

	LR1	Fox
Da	0.4883	0.148
$\omega$	0.03388	0.04
$\sigma$	$\ln(2.2)$	$\ln(1.314)$
$g$	0	$7.221 \times 10^{-5}$
$\eta$	0	0.6
$\gamma$	$2.25 \times 10^{-6}$	$8.575 \times 10^{-3}$

In both cases, the Galerkin formulations for  $p(\zeta, t)$  and  $a_{Ca}(\zeta, t)$  are approximated by 28 modes, namely  $p(\zeta, t) = \sum_{i=1}^{28} p_i(t)\phi_i(\zeta)$  and  $a_{Ca}(\zeta, t) = \sum_{i=1}^{28} a_{Ca_i}(t)\psi_i(\zeta)$ . This leads to a finite-dimensional approximation to Eq. 2.13, of the form

$$\dot{x}(t) = \bar{A}^e x(t) + \bar{B}^e u(t) \quad (2.32)$$

where  $\bar{A}^e$  and  $\bar{B}^e$  are  $(57 \times 57)$  and  $(57 \times 2)$  matrices, respectively. Increasing the number of modes in the Galerkin formulation will increase the number of fast modes, which are stable. Since the controller formulation is based only on the slow modes, increasing the total number of modes will not affect the overall result. The function  $B(\zeta)$  has the general form

$$B(\zeta) = \exp^{a\zeta} [c_1 \cos(b\zeta) + c_2 \sin(b\zeta)] \quad (2.33)$$

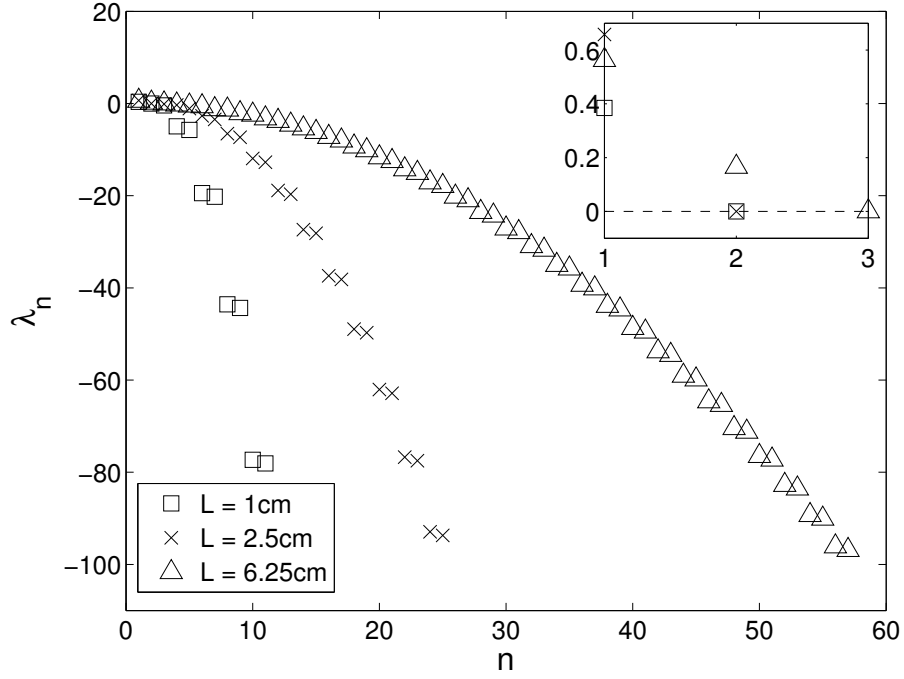


Figure 2.2: Eigenspectrum of  $\mathcal{A}^e$  for the LR1 model, for different cable lengths.

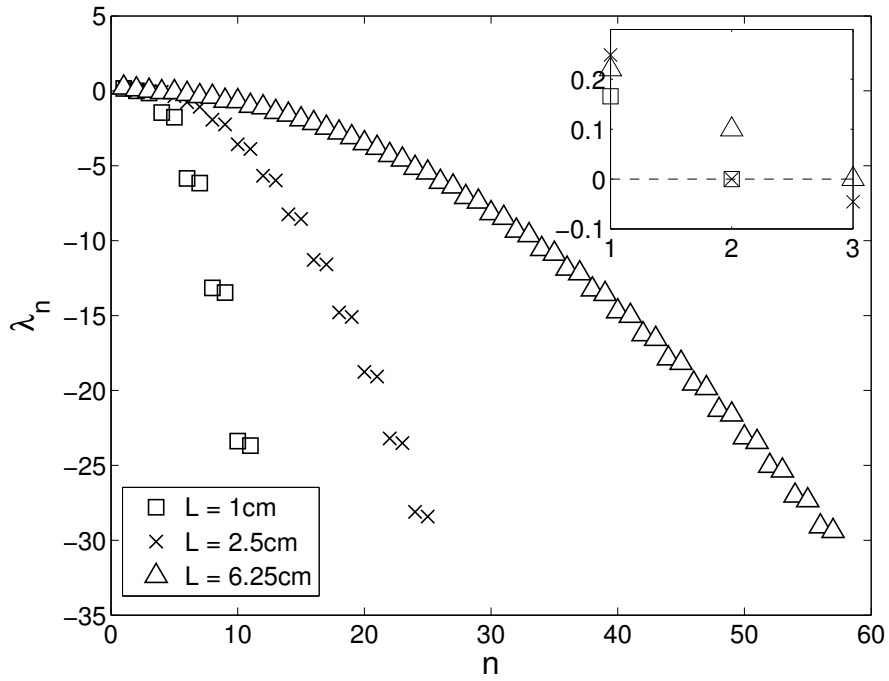


Figure 2.3: Eigenspectrum of  $\mathcal{A}^e$  for the Fox ionic model, for different cable lengths.

where  $a$  and  $b$  are the real and imaginary parts of  $r$ , which satisfy the characteristic equation of Eq. 2.2a:

$$D ar^2 - \omega r + \sigma = 0 \quad (2.34)$$

The coefficients  $c_1$  and  $c_2$  can be found by applying the following boundary conditions:

$$\left. \frac{dB}{d\zeta} \right|_{\zeta=0} - B(0) = 1 \quad \left. \frac{dB}{d\zeta} \right|_{\zeta=L} = 0 \quad (2.35)$$

The  $\text{Ca}^{2+}$ -based controller,  $u_{Ca}(t)$ , is applied at  $\zeta \in [3.5, 4.5]$  cm. The location of this actuator was chosen to be far enough from the boundary, such that its effects are independent from the boundary pacer. In choosing the size of this region, we have considered the trade-off between the magnitude of actuation and the size of the actuator. This size was therefore selected such that the magnitude of actuation is not too high, while keeping the affected region relatively small.

Once the finite-dimensional approximation of the system has been obtained, the system is decomposed into the stable (fast) and unstable (slow) subsystems. The low dimensional unstable subsystem is then used to compute the optimal control law, given by Eq. 2.30. Computation of the optimal control law requires solving the Algebraic Riccati Equation. This is done through Matlab using the 'care' function. Note that in this procedure, the nonlinear term in Eq. 2.2a is neglected. However, since this term has a stabilizing effect on the system, this exclusion has no negative effect on the stability of the closed loop system. In the simulations, this nonlinear term is added to the closed loop system as  $\mathcal{G}_i(t) = g\langle a(\zeta, t)^3, \phi_i^*(\zeta) \rangle$ . The same penalty matrices are used in both cases.  $Q$  can be partitioned as  $Q = [q_v \ 0; \ 0 \ q_a I]$ , where  $q_v = 10$  is applied to  $v(t)$  and  $q_a = 5$  is applied to  $p(t)$  and  $a_{Ca}(t)$ . For the input variables, an equal weight is placed on  $\tilde{v}(t)$  and  $u_{Ca}(t)$ :  $R = [5 \ 0; \ 0 \ 5]$ . The numerical integration is performed using the explicit finite difference method with  $\Delta t = 0.02$ .

#### 2.4.1 Case 1: LR1 ionic model

For the parameter values given in Table 2.1 and a cable length of 6.25 cm,  $\mathcal{A}^e$  has three unstable eigenvalues (including the zero eigenvalue). As discussed previously, all the unstable eigenvalues correspond to those of  $\mathcal{A}_1$ . Therefore, for the LR1 model, the  $a_{Ca}(\zeta, t)$  PDE (Eq. 2.2b) is inherently stable, and only Eq. 2.2a needs to be stabilized.

The finite-dimensional approximation of the system, Eq. 2.32, takes the form of Eq. 2.26, where  $\bar{A}^e$  and  $\bar{B}^e$  can be computed by following the procedure outlined in Eqs. 2.20 - 2.25. Since there are three unstable modes, a third-order optimal controller is obtained. Solving the LQR problem posed in Eq. 2.29, we obtained the following optimal controller gain:

$$K_{opt} = \begin{bmatrix} 1 & -23.3 & 4.61 \\ 0 & 0 & 0 \end{bmatrix} \quad (2.36)$$

As noted earlier, since the  $a_{Ca}(\zeta, t)$  system is already stable,  $u_{Ca}(t)$  is deemed unnecessary in this case, and therefore the corresponding controller gains are equal to zero. Applying this controller gain to Eq. 2.32 (via Eq. 2.30), we obtained the closed loop response for  $a(\zeta, t)$ , shown in Figure 2.4. This figure shows that the low dimensional controller can indeed stabilize all the 28 modes of  $a(\zeta, t)$ . The corresponding trajectories of  $v(t)$  and  $\tilde{v}(t)$  are shown in Figures 2.7 and 2.8.

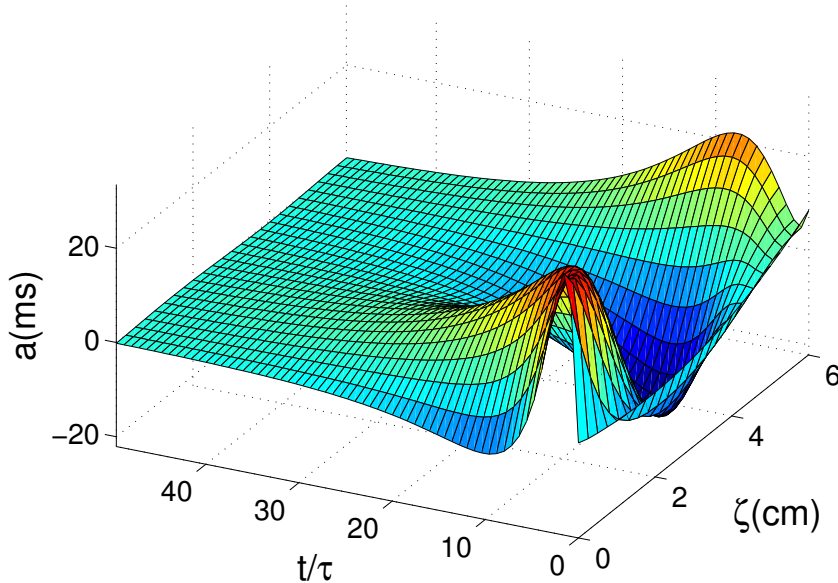


Figure 2.4: Stabilization of the amplitude of alternans PDE under optimal full-state feedback control with LR1 model parameters.

### 2.4.2 Case 2: Fox ionic model

In this case, despite the fact that all the eigenvalues of  $\mathcal{A}_2$  are negative, instabilities can still arise in the  $a_{Ca}(\zeta, t)$  system due to the bidirectional coupling between Eqs. 2.2a and 2.2b. Using the parameter values in Table 2.1, we found that  $\mathcal{A}^e$  has three unstable eigenvalues. Therefore, both  $a(\zeta, t)$  and  $a_{Ca}(\zeta, t)$  need to be stabilized.

As noted in the previous section, analytical expressions for the eigenvalues and eigenfunctions of  $\mathcal{A}^e$  are not available when  $\eta$  is nonzero. Therefore,  $\bar{A}^e$  and  $\bar{B}^e$  must be computed according to Eq. 2.28. A state transformation was then performed to diagonalize  $\bar{A}^e$  before the unstable subsystem was extracted. The remaining procedure for obtaining the optimal control law is identical to that employed in the LR1 case. Here, the optimal controller gain was found to be:

$$K_{opt} = \begin{bmatrix} 0.469 & -11.2 & 2.46 \\ -0.957 & -10.1 & 1.54 \end{bmatrix} \quad (2.37)$$

In contrast to the previous case, the second row of  $K_{opt}$  is now nonzero since the  $a_{Ca}(\zeta, t)$  system is also unstable. Figures 2.5 and 2.6 show the stabilization of  $a(\zeta, t)$  and  $a_{Ca}(\zeta, t)$ , respectively, under this optimal control law. Again, these figures demonstrate that stabilization of all the 28 modes of  $a(\zeta, t)$  and  $a_{Ca}(\zeta, t)$  can be achieved using the low-dimensional optimal controller. The input trajectories  $v(t)$ ,  $\tilde{v}(t)$  and  $u_{Ca}(t)$  are shown in Figures 2.7 - 2.9.

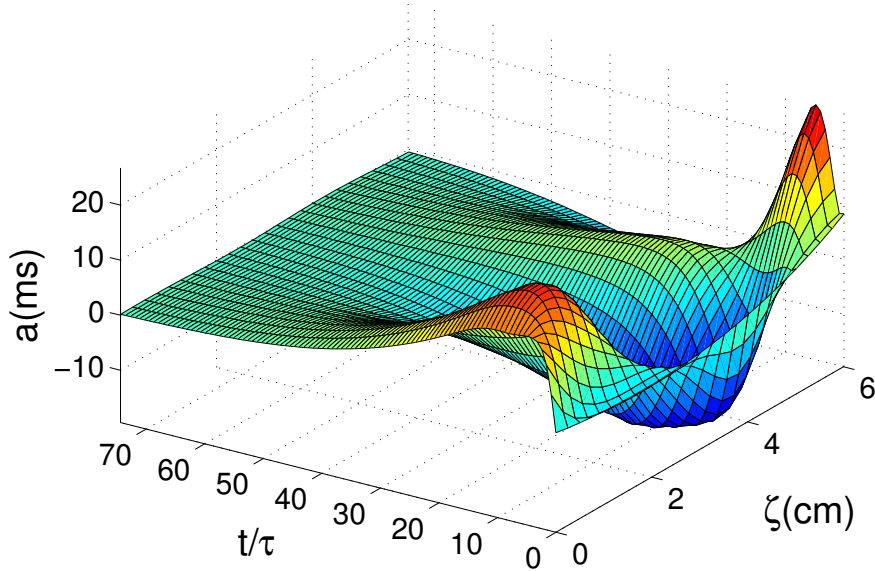


Figure 2.5: Stabilization of the amplitude of alternans PDE under optimal full-state feedback control with Fox model parameters.

It is important to note that although the exponential stabilization of the infinite-dimensional state variables is achieved in both cases, this method does not account for the influence of the feedback control law on the higher (fast) modes. In reality, the higher modes of  $\mathcal{A}^e$  may be amplified by the control law. This is known as the spillover effect [34]. In the simulations, this phenomena is reflected as the high excursion of the state variables away from the boundary pacing site, as shown in Figures 2.4 - 2.6.

From Figures 2.7 and 2.8, it is apparent that the boundary controller for the LR1 model is significantly more aggressive compared to that for the Fox model. This is because for the LR1 model, the stabilization of  $a(\zeta, t)$  must be achieved solely through boundary control. On the other hand, for the Fox model, stabilization is achieved using both boundary and spatial actuations, and as a result aggressive controller actions are not required. This is advantageous for the implementation

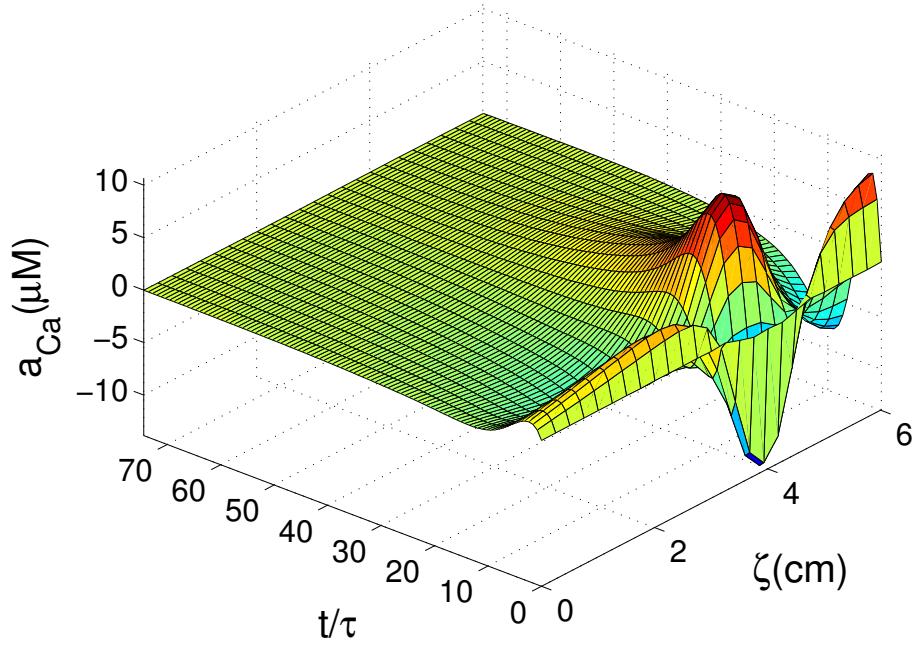


Figure 2.6: Stabilization of the amplitude of calcium alternans PDE under optimal full-state feedback control with Fox model parameters.

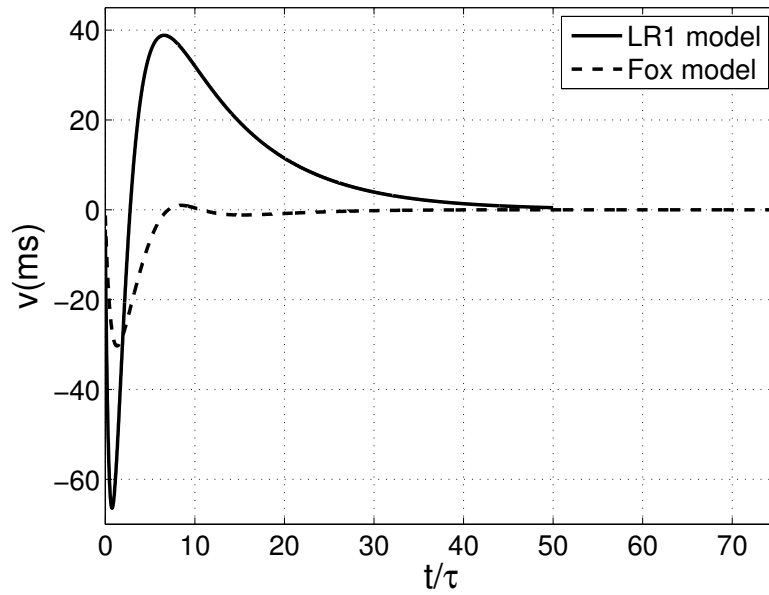


Figure 2.7: Trajectories of boundary input  $v(t)$  for the LR1 and Fox ionic models under optimal full-state feedback control.

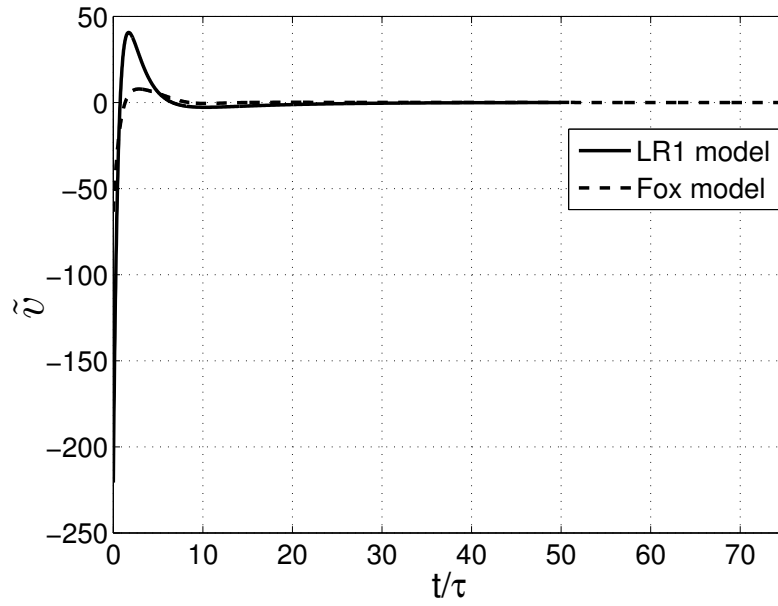


Figure 2.8: Trajectories of input derivative  $\tilde{v}(t)$  for the LR1 and Fox ionic models under optimal full-state feedback control.

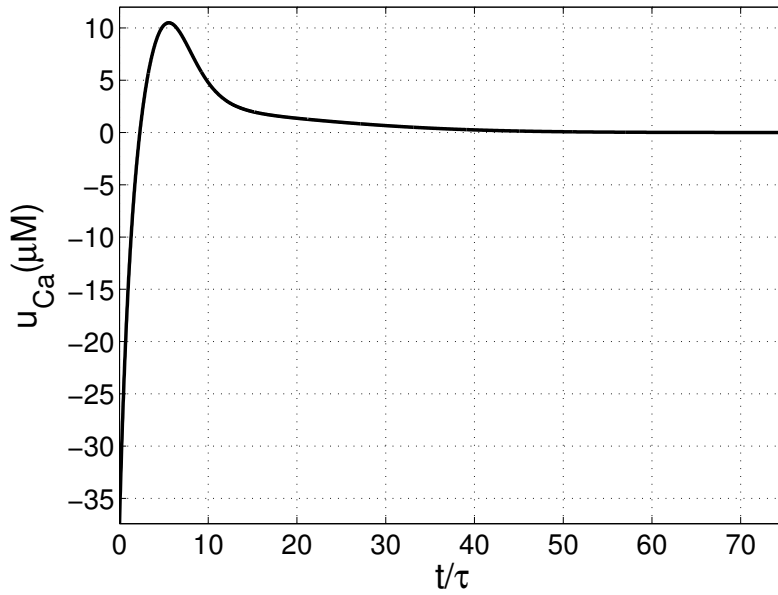


Figure 2.9: Trajectory of  $u_{Ca}(t)$  for the Fox ionic model under optimal full-state feedback control.

of the control scheme, since an overly aggressive boundary controller may result in conduction block, which is highly undesirable.

The results obtained from the LR1 model imply that in the case of full-state feedback realization (i.e. full knowledge of the APD state evolution), boundary pacing alone can potentially stabilize alternans along the entire length of the cable. However, in reality this cannot be achieved, because it is impossible to measure the electrical activity at each cardiac cell within the domain.

An important limitation for the boundary actuator is the fact that the pacing protocol should not postpone the heart's natural rhythm, which is governed by the sinoatrial node (SAN). In other words, the boundary actuation is constrained to negative perturbations only. This provides the motivation to extend this work further into the framework of model predictive control, such that input constraints can be explicitly accounted for in the controller formulation.

## 2.5 Conclusion

In this chapter, an optimal full-state feedback control scheme was developed for the coupled system of PDEs describing the dynamics of the small amplitude of cardiac alternans and the peak intracellular  $\text{Ca}^{2+}$  concentration alternations along a 1D cable of cardiac cells. This control scheme combines a pacer applied at the boundary and a spatially distributed,  $\text{Ca}^{2+}$ -based controller. The optimal control law was obtained by solving the standard LQR problem. Simulations were performed using PDE parameters obtained from the LR1 ionic model and the Fox ionic model. In both cases, we demonstrated the successful annihilation of cardiac alternans along a 6.25 cm cable of cardiac cells. The annihilation of cardiac alternans using feedback control has been studied extensively. However, it has been shown in literature that control strategies that are solely voltage-based are only effective close to the control site. Away from the pacing site, alternans will continue growing, eventually leading to conduction block. In this work, we have demonstrated that by the inclusion of a voltage-independent actuator (i.e. calcium-based), we can overcome this limitation in controllability, and achieve alternans annihilation along the entire cable. In developing these control strategies, constraints that may be naturally present in the cardiac system were not accounted for. This issue will be addressed in the next chapter, where the input and state constraints are to be included explicitly in the controller formulation.

## Chapter 3

# Model predictive control of the amplitude of alternans PDE

### 3.1 Introduction

In this chapter, we develop a model predictive controller (MPC) for the small amplitude of alternans PDE [31]. The control strategy is implemented as a combination of boundary actuation and spatially distributed,  $\text{Ca}^{2+}$ -based actuation. This PDE belongs to a class of parabolic PDEs that describe diffusion-convection-reaction processes, which can be transformed into an infinite dimensional abstract evolutionary form [32, 33]. Similar to optimal control, which is studied in the previous chapter, the MPC algorithm also involves minimizing a quadratic cost function. However, in MPC this minimization is performed at every time step. Furthermore, MPC allows the explicit inclusion of input and state constraints into the minimization problem. This makes it a popular option for processes in which constraints are present. MPC and its properties (i.e. stability, performance, constraints handling, etc.) have been studied extensively in literature [37–39]. However, most of the resulting MPC formulations are developed for lumped-parameter models, which are finite-dimensional.

There are previous studies that address MPC for infinite dimensional systems arising from PDEs [40–43]. The approach in [42] involve on-line model reduction and linearization, while [43] makes use of the system’s dissipativity to formulate a plant-wide distributed model predictive control (DMPC) algorithm. In this work, based on the approach used in [40, 41], the infinite dimensional system is partitioned into slow (finite dimensional) and fast (infinite dimensional) subsystems, from which a low order, finite dimensional MPC can be constructed using one of the existing MPC formulations. Input constraint satisfaction is achieved using this low-order MPC formulation, while state constraints satisfaction requires a correction factor that accounts for the evolution of the fast subsystem. In the cardiac system, these constraints are important for avoiding conduction block

in the tissue.

This chapter is organized as follows. Section 3.2 introduces the amplitude of alternans PDE and the system's state space representation. The MPC formulation is presented in Section 3.3, and a numerical example is given in Section 3.4. Finally, a brief summary is provided in Section 3.5.

## 3.2 Model description

In this chapter, we only consider the amplitude of APD alternans PDE [31], which is given by Eq. 2.2a in the previous chapter. Since we are only working with a single PDE, the  $\text{Ca}^{2+}$ -based actuation is applied directly to this PDE. The system is therefore given by:

$$\frac{\partial a(\zeta, t)}{\partial t} = \text{Da} \frac{\partial^2 a(\zeta, t)}{\partial \zeta^2} - \omega \frac{\partial a(\zeta, t)}{\partial \zeta} + \sigma a(\zeta, t) - ga(\zeta, t)^3 + h \sum_{j=1}^m b_j(\zeta) u_{Ca_j}(t) \quad (3.1a)$$

$$\frac{\partial a(0, t)}{\partial \zeta} = a(0, t) + v(t), \quad \frac{\partial a(L, t)}{\partial \zeta} = 0 \quad (3.1b)$$

$$a(\zeta, 0) = a_0(\zeta) \quad (3.1c)$$

All parameters are normalized with respect to the pacing period  $\tau$ . Definitions for  $\text{Da}$ ,  $\omega$ ,  $\sigma$  and  $g$  can be found in [31], and are also given in Chapter 2. The parameter  $h$  represents a proportionality factor between the change in the peak intracellular  $[\text{Ca}^{2+}]$  and the change in  $a(\zeta, t)$ . The magnitude of  $h$  can be obtained by following the same procedure used to obtain the coupling parameter  $\eta$  in the previous chapter.

In Eq. 3.1a,  $u_{Ca}(t)$  denotes the spatially distributed,  $\text{Ca}^{2+}$ -based control input. The spatial distribution of  $u_{Ca_j}(t)$  along the cable is given by the function  $b_j(\zeta)$ , and the summation term represents the overall effect of the calcium-based actuator(s) on the system.  $b_j(\zeta)$  is a square integrable function, and is defined as  $b_j(\zeta) = \frac{1}{2\nu}$  for  $\zeta \in [\zeta_{b,j} - \nu, \zeta_{b,j} + \nu]$  and zero everywhere else, where  $\zeta_{b,j}$  denotes the location of the  $j^{\text{th}}$  distributed actuator and  $\nu$  is a small positive real number. In Eq. 3.1b,  $v(t)$  denotes the boundary actuator applied at  $\zeta = 0$ . This boundary actuator represents a pacing protocol applied at the end of the cable. The  $\text{Ca}^{2+}$ -based actuator is applied locally on the cable and manipulates the intracellular  $\text{Ca}^{2+}$  concentration in that region. This can be achieved by applying either a drug patch or a mechanical perturbation to the heart tissue.

The output, which represents the measurement of  $a(\zeta, t)$  at  $\zeta_c$ , is defined as

$$y(t) = \int_0^L r(\zeta) a(\zeta, t) d\zeta \quad (3.2)$$

The function  $r(\zeta)$  is defined similarly as  $b_j(\zeta)$ , and is given by  $r(\zeta) = \frac{1}{2\delta}$  for  $\zeta \in [\zeta_c - \delta, \zeta_c + \delta]$  and zero everywhere else.

### 3.2.1 State space system representation

Following the same procedure outlined in Chapter 2, the system given by Eq. 3.1 can be represented as an infinite dimensional state space system. The PDE given by Eq. 3.1 has a spatially uniform unstable steady state at  $a(\zeta, t) = 0$ . After linearizing the PDE around this point, the system can be formulated as the following abstract boundary control problem:

$$\begin{aligned}\frac{da}{dt} &= \mathcal{F}a(t) + \mathcal{B}_{C_a}u_{C_a}(t) & t \geq 0 \\ a(0) &= a_0 \\ \mathcal{B}a(t) &= v(t)\end{aligned}\tag{3.3}$$

Where  $a(\cdot, t) = \{a(\zeta, t), 0 \leq \zeta \leq L\}$  is the state variable in the Hilbert space  $\mathcal{L}_2([0, L]; t)$  [32],  $t$  is the time variable,  $v(t) \in \mathbb{R}$  is the boundary actuation and  $u_{C_a}(t)$  is the spatially distributed actuation.  $\mathcal{F}$  is the spatial derivative operator and is defined in Eq. 2.4. Compared to the previous chapter, the definition for  $\mathcal{B}_{C_a}$ , which describes the positioning of the spatially distributed actuator, is modified slightly to incorporate the proportionality factor  $h$ :

$$\mathcal{B}_{C_a}u_{C_a}(t) = h \sum_{j=1}^m b_j(\zeta)u_{C_{a_j}}(t)\tag{3.4}$$

Since there is only one spatially distributed actuator, the index  $j$  will be dropped. Finally, the boundary operator  $\mathcal{B} : L_2(0, L) \mapsto \mathbb{R}$  is defined in Eq. 2.5.

In Eq. 3.3, the controlled input,  $v(t)$ , appears in the boundary condition. We want to find an exact transformation such that  $v(t)$  is moved from the boundary into the spatial domain of the PDE. This transformation is given by Eq. 2.8, and is based on the assumption that  $v(t)$  is sufficiently smooth and that there exists a function  $B(\zeta)$  such that  $\forall v(t)$ ,  $B(\zeta)v(t) \in \mathcal{D}(\mathcal{F})$ , and Eq. 2.7 is satisfied. We then define a new operator,  $\mathcal{A}$ :

$$\mathcal{A}\phi(\zeta) = \mathcal{F}\phi(\zeta), \text{ and } \mathcal{D}(\mathcal{A}) = \mathcal{D}(\mathcal{F}) \cup \ker(\mathcal{B})\tag{3.5}$$

By applying the boundary transformation, we obtain the following:

$$\begin{aligned}\frac{\partial p(\zeta, t)}{\partial t} &= \mathcal{A}p(\zeta, t) + \mathcal{F}B(\zeta)v(t) - B(\zeta)\dot{v}(t) + \mathcal{B}_{C_a}u_{C_a}(t) & t \geq 0 \\ p(\zeta, 0) &= p_0(\zeta)\end{aligned}\tag{3.6}$$

Defining  $v(t)$  as a new state variable, the system given by Eq. 3.1 is reformulated on the extended state space  $\mathcal{L}_2^e := \mathcal{L}_2 \otimes V$ , yielding

$$\begin{aligned}\begin{bmatrix} \dot{v}(t) \\ \dot{p}(\zeta, t) \end{bmatrix} &= \begin{bmatrix} 0 & 0 \\ \mathcal{F}B & \mathcal{A} \end{bmatrix} \begin{bmatrix} v(t) \\ p(\zeta, t) \end{bmatrix} + \begin{bmatrix} 1 & 0 \\ -B & \mathcal{B}_{C_a} \end{bmatrix} \begin{bmatrix} \tilde{v}(t) \\ u_{C_a}(t) \end{bmatrix} \\ &= \mathcal{A}^e x(\zeta, t) + \mathcal{B}^e u(t)\end{aligned}\tag{3.7}$$

Here,  $\tilde{v}(t) = \dot{v}(t)$ . Physiologically,  $\tilde{v}(t)$  can be interpreted as the rate of change of pacing period applied at the boundary. Furthermore, without loss of generality, we can choose  $B(\zeta)$  such that  $\mathcal{F}B(\zeta) = 0$ . By doing this,  $\dot{v}(t)$  becomes independent of  $p(\zeta, t)$ .

The operator  $\mathcal{A}$  is the Sturm-Liouville operator. Its eigenvalues and corresponding eigenfunctions can be found analytically by solving the eigenvalue problem  $\mathcal{A}\phi(\zeta) = \lambda\phi(\zeta)$ , through the separation of variables [32]. The eigenfunctions of the adjoint operator  $\mathcal{A}^*$  that satisfies the orthogonality condition  $\langle \phi_m(\zeta), \phi_n^*(\zeta) \rangle = \delta_{mn}$  can also be computed. The eigenvalues of  $\mathcal{A}$  are given by:

$$\lambda_n = \sigma - \text{Da} \left[ \alpha_n + \frac{w^2}{4\text{Da}^2} \right], 0 < \alpha_n < \alpha_{n+1}, n \geq 1 \quad (3.8)$$

where  $\alpha_n$ 's are solutions to the following transcendental equation:

$$\tan(\sqrt{\alpha_n}L) = \frac{\sqrt{\alpha_n}}{\alpha_n - \frac{\omega}{2\text{Da}} \left(1 - \frac{\omega}{2\text{Da}}\right)} \quad (3.9)$$

The corresponding eigenfunctions and adjoint eigenfunctions for  $n \geq 1$  are given by:

$$\phi_n(\zeta) = B_n \exp^{\frac{\omega}{2\text{Da}}\zeta} \left[ \cos(\sqrt{\alpha_n}\zeta) + \frac{1}{\sqrt{\alpha_n}} \left(1 - \frac{\omega}{2\text{Da}}\right) \sin(\sqrt{\alpha_n}\zeta) \right] \quad (3.10a)$$

$$\phi_n^*(\zeta) = \exp^{-\frac{\omega}{\text{Da}}\zeta} \phi_n(\zeta) \quad (3.10b)$$

The coefficients  $B_n$ 's are computed by imposing the orthogonality condition between  $\phi_n(\zeta)$  and  $\phi_n^*(\zeta)$ , and are evaluated as:

$$B_n = \left\{ \int_0^L \left[ \cos(\sqrt{\alpha_n}\zeta) + \frac{1}{\sqrt{\alpha_n}} \left(1 - \frac{\omega}{2\text{Da}}\right) \sin(\sqrt{\alpha_n}\zeta) \right]^2 d\zeta \right\}^{-1/2} \quad (3.11)$$

Parabolic PDEs such as the one given by Eq. 3.1 can be solved by modal decomposition [33]. In this approach,  $p(\zeta, t)$  is written as the infinite sum  $p(\zeta, t) = \sum_{n=1}^{\infty} p_n(t)\phi_n(\zeta)$ . Substituting this into Eq. 3.7 and projecting the resulting system onto  $\phi_n^*(\zeta)$ , we obtain:

$$\begin{aligned} \begin{bmatrix} \dot{v}(t) \\ \dot{p}_n(t) \end{bmatrix} &= \begin{bmatrix} 0 & 0 \\ 0 & \lambda_n \end{bmatrix} \begin{bmatrix} v(t) \\ p_n(t) \end{bmatrix} + \begin{bmatrix} 1 & 0 \\ -\langle B, \phi_n^* \rangle & h\langle b, \phi_n^* \rangle \end{bmatrix} \begin{bmatrix} \tilde{v}(t) \\ u_{Ca}(t) \end{bmatrix}, \quad n \geq 1 \\ \dot{x}(t) &= A^e x(t) + B^e u(t) \end{aligned} \quad (3.12)$$

since  $\mathcal{F}B(\zeta) = 0$ . Following a similar procedure, the state space representation for Eq. 3.2 can be derived as:

$$y(t) = \left[ \langle r(\zeta), B(\zeta) \rangle \quad \langle r(\zeta), \phi_n(\zeta) \rangle \right] x(t) = Cx(t), \quad n \geq 1 \quad (3.13)$$

This is the infinite dimensional state space representation for the system given by Eqs. 3.1 - 3.2.

### 3.3 Model Predictive Control

In this work, we utilize the MPC formulation developed by Muske and Rawlings [38]. Although the approach in [38] was developed for finite dimensional systems, here we are using their framework to address an infinite dimensional system representation. The eigenspectra of dissipative, parabolic PDEs such as Eq. 3.1a, has a beneficial structure which allows for the formulation of a simple control law which stabilizes the unstable modes, while the stable modes remain invariant to the control law. The eigenspectrum of  $\mathcal{A}^e$  can be divided into a finite-dimensional unstable (slow) part and an infinite-dimensional stable (fast) part, i.e.  $\Omega(\mathcal{A}^e) = \Omega^+(\mathcal{A}^e) \cup \Omega^-(\mathcal{A}^e)$ . Since the dominant dynamics of the PDE are captured in the slow subsystem, the finite-dimensional MPC is developed based on this subsystem, yielding a stabilizing, low-order predictive controller for the entire infinite dimensional system.

#### System discretization

In order to apply the MPC formulation, the system given by Eq. 3.12 must first be discretized. To ensure that the system's fastest dynamics are not lost in the discretization, the sampling interval is chosen such that  $\Delta t \leq \frac{1}{2|\lambda_n|_{\max}}$ . For finite dimensional systems, the continuous-time system representation can be discretized exactly. However, this involves taking the exponential of the state evolution matrix. For infinite dimensional systems, one approach is to employ the Tustin time discretization scheme, which utilizes the Cayley transform [44]. This method is based on a modified Crank-Nicholson type discretization scheme. The discrete-time representation of Eqs. 3.12 - 3.13 is given by:

$$\bar{x}(k+1) = \bar{A}\bar{x}(k) + \bar{B}\bar{u}(k), \quad (3.14a)$$

$$y(k) = C\bar{x}(k) \quad (3.14b)$$

$\bar{A}$  and  $\bar{B}$  are defined as follows:

$$\bar{A} = (\mu I - A^e)^{-1}(\mu I + A^e) \quad (3.15a)$$

$$\bar{B} = \sqrt{2\mu}(\mu I - A^e)^{-1}B^e \quad (3.15b)$$

where  $\mu = \frac{2}{\Delta t}$  and  $I$  is the identity matrix. In this transformation, the stable (unstable) eigenvalues of  $A^e$ , which lie on the left (right) half plane, are mapped onto the interior (exterior) of the unit circle. In addition to this transformation from continuous to discrete-time infinite dimensional system representation, the Cayley transformation maps the unbounded operators  $A^e$  and  $B^e$  into their bounded, infinite dimensional counterparts  $\bar{A}$  and  $\bar{B}$ , respectively [45].

Equation 3.14 can then be partitioned into a slow and a fast subsystem, according to the eigenspectrum of  $\bar{A}$ . These subsystems are given by:

$$\bar{x}_s(k+1) = \bar{A}_s \bar{x}_s(k) + \bar{B}_s \bar{u}(k) \quad (3.16a)$$

$$\bar{x}_f(k+1) = \bar{A}_f \bar{x}_f(k) + \bar{B}_f \bar{u}(k) \quad (3.16b)$$

$$y_s(k) = C_s \bar{x}_s(k) \quad (3.16c)$$

$$y_f(k) = C_f \bar{x}_f(k), \quad k \geq 0 \quad (3.16d)$$

In Eqs. 3.16a and 3.16c, the state variables are  $\bar{x}_s(k) = [v(k) \ p_s(k)]'$ , while in Eqs. 3.16b and 3.16d,  $\bar{x}_f(k) = p_f(k)$ . The subscripts  $s$  and  $f$  denote slow and fast modes, respectively. Note that for the MPC formulation to be feasible, the slow subsystem must contain at least one stable mode.

### 3.3.1 Controller formulation

The MPC computes a sequence of  $N$  future inputs that will minimize the following infinite horizon open-loop quadratic objective function at each time instant  $k$ :

$$\min_{\bar{u}^N} J_\infty(k) = \sum_{j=0}^{\infty} [\bar{x}_s(k+j)' Q \bar{x}_s(k+j) + \bar{u}(k+j)' R \bar{u}(k+j)] \quad (3.17)$$

Here,  $Q \geq 0$  and  $R > 0$  are symmetric penalty matrices for the state and input variables, respectively.

The vector  $\bar{u}^N$  contains the  $N$  future control moves that will minimize the cost function, i.e.  $\bar{u}^N = [\bar{u}(k) \ \bar{u}(k+1) \ \dots \ \bar{u}(k+N-1)]'$ . For all  $j \geq N$ ,  $\bar{u}(k+j)$  is set to zero. At each time step, the first control move  $\bar{u}(k)$  is applied to the plant model, and  $\bar{u}^N$  is recalculated using the updated state vector. Equation 3.17 can be represented as the finite horizon open-loop objective function:

$$\min_{\bar{u}^N} J_N(k) = \bar{x}_s(k+N)' \bar{Q} \bar{x}_s(k+N) + \sum_{j=0}^{N-1} [\bar{x}_s(k+j)' Q \bar{x}_s(k+j) + \bar{u}(k+j)' R \bar{u}(k+j)] \quad (3.18)$$

In Eq. 3.18,  $\bar{Q}$  is the terminal state penalty matrix, whose formulation depends on the stability of the system [38].

In this work, the system is unstable. Thus, the Jordan form of  $\bar{A}_s$  must first be partitioned into stable and unstable parts:

$$\bar{A}_s = V J V^{-1} = \begin{bmatrix} V_u & V_s \end{bmatrix} \begin{bmatrix} J_u & 0 \\ 0 & J_s \end{bmatrix} \begin{bmatrix} \tilde{V}_u \\ \tilde{V}_s \end{bmatrix} \quad (3.19)$$

where the subscripts  $u$  and  $s$  correspond to the unstable and stable parts, respectively. For unstable systems,  $\bar{Q}$  is computed as

$$\bar{Q} = \tilde{V}_s' \Sigma \tilde{V}_s \quad (3.20a)$$

$$\Sigma = V_s' Q V_s + J_s' \Sigma J_s \quad (3.20b)$$

Algebraic manipulation of Eq. 3.18 leads to the following quadratic program for  $\bar{u}^N$ .

$$\min_{\bar{u}^N} J_N(k) = \left[ (\bar{u}^N)' H \bar{u}^N + 2(\bar{u}^N)' G \bar{x}_s(k) \right] \quad (3.21)$$

For unstable systems,  $H$  and  $G$  are given by:

$$H_1 = \begin{bmatrix} \bar{B}'_s K_{N-1} \bar{B}_s + R & \bar{B}'_s \bar{A}'_s K_{N-2} \bar{B} & \cdots & \bar{B}'_s \bar{A}'_s{}^{N-1} K_0 \bar{B}_s \\ \bar{B}'_s K_{N-2} \bar{A}_s \bar{B}_s & \bar{B}'_s K_{N-2} \bar{B}_s + R & \cdots & \bar{B}'_s \bar{A}'_s{}^{N-2} K_0 \bar{B}_s \\ \vdots & \vdots & \ddots & \vdots \\ \bar{B}'_s K_0 \bar{A}_s^{N-1} \bar{B}_s & \bar{B}'_s K_0 \bar{A}_s^{N-2} \bar{B}_s & \cdots & \bar{B}'_s K_0 \bar{B}_s + R \end{bmatrix} \quad (3.22a)$$

$$G_1 = \begin{bmatrix} \bar{B}'_s K_{N-1} \bar{A}_s \\ \vdots \\ \bar{B}'_s K_0 \bar{A}_s^N \end{bmatrix}, \quad K_N = \sum_{i=0}^N \bar{A}_s^{i} Q \bar{A}_s^i \quad (3.22b)$$

$$H_2 = \begin{bmatrix} \bar{B}'_s L_{N-1} \bar{B}_s & \bar{B}'_s \bar{A}'_s L_{N-2} \bar{B}_s & \cdots & \bar{B}'_s \bar{A}'_s{}^{N-1} L_0 \bar{B}_s \\ \bar{B}'_s L_{N-2} \bar{A}_s \bar{B}_s & \bar{B}'_s L_{N-2} \bar{B}_s & \cdots & \bar{B}'_s \bar{A}'_s{}^{N-2} L_0 \bar{B}_s \\ \vdots & \vdots & \ddots & \vdots \\ \bar{B}'_s L_0 \bar{A}_s^{N-1} \bar{B}_s & \bar{B}'_s L_0 \bar{A}_s^{N-2} \bar{B}_s & \cdots & \bar{B}'_s L_0 \bar{B}_s \end{bmatrix} \quad (3.22c)$$

$$G_2 = \begin{bmatrix} \bar{B}'_s L_{N-1} \bar{A}_s \\ \vdots \\ \bar{B}'_s L_0 \bar{A}_s^N \end{bmatrix}, \quad L_N = \bar{A}_s^{iN} \bar{Q} \bar{A}_s \quad (3.22d)$$

$$H = H_1 + H_2 \quad (3.22e)$$

$$G = G_1 + G_2 \quad (3.22f)$$

Since Eq. 3.21 is based only on the slow subsystem, the solution to the optimization problem is only sub-optimal with respect to the whole, infinite dimensional system. However, stabilization of the whole system will still be achieved.

### 3.3.2 Constraints

The main advantage of MPC is the ability to explicitly incorporate input and state constraints into the controller formulation. Here, we wish to apply constraints to  $u_{Ca}(t)$ ,  $v(t)$  and  $a(\zeta, t)$  measured over the region  $\zeta \in [\zeta_c - \delta, \zeta_c + \delta]$ ,  $\delta > 0$  (i.e.  $y(t)$ ). Since the MPC is constructed based on the extended state space system (Eq. 3.12), constraints on  $y(t)$  and  $v(t)$  are treated as state (output) constraints, while those for  $u_{Ca}(t)$  are treated as input constraints.

The input and state constraints can be formulated as follows:

$$u_{\min} \leq u_{Ca}(k+j) \leq u_{\max}, \quad j = 0, \dots, N-1 \quad (3.23a)$$

$$v_{\min} \leq v(k+j) \leq v_{\max}, \quad j = j_1, \dots, j_2 \quad (3.23b)$$

$$y_{\min} \leq y(k+j) \leq y_{\max}, \quad j = \tilde{j}_1, \dots, \tilde{j}_2 \quad (3.23c)$$

where  $\{j_1, \tilde{j}_1\} \geq 1$  and  $\{j_2, \tilde{j}_2\} \geq \{j_1, \tilde{j}_1\}$ . Through algebraic manipulation, Eq. 3.23 can be rewritten as an inequality in terms of  $\bar{u}^N$ :

$$\begin{bmatrix} I \\ -I \\ D_v \\ -D_v \\ D \\ -D \end{bmatrix} \bar{u}^N \leq \begin{bmatrix} i_1 \\ i_2 \\ v_1 \\ v_2 \\ d_1 \\ d_2 \end{bmatrix} \quad (3.24)$$

where  $I$  is the identity matrix, and

$$D = \begin{bmatrix} C_s \bar{A}_s^{\tilde{j}_1-1} \bar{B}_s & \dots & C_s \bar{A}_s^{\tilde{j}_1-N} \bar{B}_s \\ \vdots & & \vdots \\ C_s \bar{A}_s^{\tilde{j}_2-1} \bar{B}_s & \dots & C_s \bar{A}_s^{\tilde{j}_2-N} \bar{B}_s \end{bmatrix}, \text{ where } \bar{A}_s^{j-i} = 0 \text{ if } j < i. \quad (3.25a)$$

For  $D_v$ , only rows  $j_1$  to  $j_2$  are nonzero. For each of these rows, the entries are equal to  $b_1$ , which is the first row of  $\bar{B}_s$ , repeated by the row number. For example, if  $j_1 = 2$  and  $j_2 = 3$ ,  $D_v$  is given by:

$$D_v = \begin{bmatrix} 0 & 0 & 0 & \dots & 0 \\ b_1 & b_1 & 0 & \dots & 0 \\ b_1 & b_1 & b_1 & \dots & 0 \\ \vdots & \vdots & \vdots & \vdots & \vdots \\ 0 & 0 & 0 & \dots & 0 \end{bmatrix} \quad (3.25b)$$

For the terms on the right hand side of the inequality,

$$i_1 = \begin{bmatrix} u_{\max} \\ \vdots \\ u_{\max} \end{bmatrix}, \quad i_2 = \begin{bmatrix} -u_{\min} \\ \vdots \\ -u_{\min} \end{bmatrix} \quad (3.25c)$$

$$v_1 = \begin{bmatrix} v_{\max} - v(k) \\ \vdots \\ v_{\max} - v(k) \end{bmatrix}, \quad v_2 = \begin{bmatrix} -v_{\min} + v(k) \\ \vdots \\ v_{\min} + v(k) \end{bmatrix} \quad (3.25d)$$

$$d_1 = \begin{bmatrix} y_{\max} - C_s \bar{A}_s^{\tilde{j}_1} \bar{x}_s(k) \\ \vdots \\ y_{\max} - C_s \bar{A}_s^{\tilde{j}_2} \bar{x}_s(k) \end{bmatrix}, \quad d_2 = \begin{bmatrix} -y_{\min} + C_s \bar{A}_s^{\tilde{j}_1} \bar{x}_s(k) \\ \vdots \\ -y_{\min} + C_s \bar{A}_s^{\tilde{j}_2} \bar{x}_s(k) \end{bmatrix} \quad (3.25e)$$

At each time step,  $\bar{u}^N$  is computed by solving Eq. 3.21, subject to the inequality constraint given by Eq. 3.24 and the equality constraint  $\bar{x}_s(k+N) = 0$ . This equality constraint ensures that the unstable modes are stabilized at time  $k+N$ . In terms of  $\bar{u}^N$  and  $\bar{x}_s(k)$ , this equality constraint can be written as:

$$\begin{aligned} \tilde{V}_u \begin{bmatrix} \bar{A}_s^{N-1} \bar{B}_s & \bar{A}_s^{N-2} \bar{B}_s & \cdots & \bar{B}_s \end{bmatrix} \bar{u}^N = -\tilde{V}_u \bar{A}_s^N \bar{x}_s(k) \\ A_{eq} \bar{u}^N = b_{eq} \end{aligned} \quad (3.26)$$

Although the low-order MPC is stabilizing, it does not guarantee state constraints satisfaction. This is because in solving the optimization problem, at each sampling time the algorithm only takes the value of  $\bar{x}_s$  (and therefore  $y_s(k)$ ), thus neglecting the evolution of the fast modes. In order to satisfy the constraints on  $y(k)$ , [40] has demonstrated that the contribution of the fast modes must also be accounted for. This is achieved by shrinking the bounds on  $y_s$ , based on the input-output boundedness of the fast subsystem. The revised state constraints are given by

$$\begin{aligned} y_{\min} + \alpha \leq y_s(k+j) \leq y_{\max} - \alpha \\ s_{\min} \leq y_s(k+j) \leq s_{\max}, \quad j = \tilde{j}_1, \dots, \tilde{j}_2 \end{aligned} \quad (3.27)$$

where  $\alpha$  is a positive real number. In the implementation,  $y_{\max}$  and  $y_{\min}$  in Eq. 3.25e are replaced with  $s_{\min}$  and  $s_{\max}$ , respectively.

### 3.4 Numerical Simulation

In our simulation study, we consider the PDE given by Eq. 3.1 with parameters obtained from the Fox ionic model [35]. Values for these parameters are as follows:  $Da = 0.148$ ,  $\omega = 0.04$ ,  $\sigma = \ln(1.314)$ ,  $g = 7.221 \times 10^{-5}$  and  $h = 0.6$ . The eigenvalues and corresponding eigenfunctions for  $\mathcal{A}$  are computed according to Eqs. 3.8 - 3.11. The eigenspectrum of  $\mathcal{A}^e$  can then be obtained as  $\Omega\{\mathcal{A}^e\} = \{0\} \cup \Omega(\mathcal{A})$ . The distribution of  $\mathcal{A}^e$ 's eigenspectrum is dependent on the cable length  $L$ . As shown in Fig. 3.1, the number of unstable eigenvalues increases with increasing cable length. In this study, we consider a cable length of 6.25 cm.

The Galerkin formulation for  $p(\zeta, t)$  is approximated using 44 modes, namely  $p(\zeta, t) \simeq \sum_{n=1}^{44} p_n(t) \phi_n(\zeta)$ , leading to a finite dimensional approximation to Eq. 3.12, where the extended state variable  $x(t)$  has 45 elements. The function  $B(\zeta)$  has the general form

$$B(\zeta) = \exp^{a\zeta} [c_1 \cos(b\zeta) + c_2 \sin(b\zeta)]$$

where  $a$  and  $b$  are the real and imaginary parts of  $r$ , which satisfy the characteristic equation of Eq.3.1a:

$$Dar^2 - \omega r + \sigma = 0$$

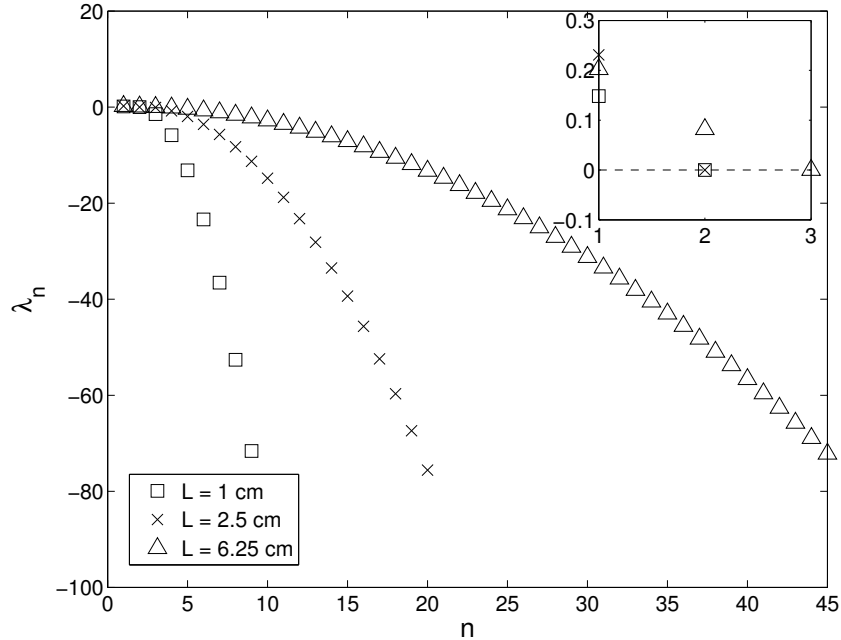


Figure 3.1: Eigenspectrum of  $\mathcal{A}^e$  for different cable lengths

The coefficients  $c_1$  and  $c_2$  can be found by applying the following boundary conditions:

$$\frac{dB}{d\zeta} \Big|_{\zeta=0} - B(0) = 1 \quad \frac{dB}{d\zeta} \Big|_{\zeta=L} = 0$$

One  $\text{Ca}^{2+}$ -based controller,  $u_{Ca}(t)$ , is applied at  $\zeta \in [4.0, 4.5]$  cm.

Once the finite-dimensional approximation of the system has been obtained, it is discretized and decomposed into stable (fast) and unstable (slow) subsystems. The low-dimensional slow subsystem is then used in the MPC synthesis. Sampling time for the discretization is computed as  $\Delta t = 0.0069$ . For a cable length of 6.25 cm,  $\mathcal{A}$  has two unstable eigenvalues, as seen in Fig. 3.1. For the extended state space system, there is an additional zero eigenvalue, which also need to be stabilized. Finally, to ensure that the optimization problem (3.21) is feasible, one additional stable mode is included in the slow subsystem. Therefore, the slow subsystem contains four state variables. The state penalty matrix can be partitioned as follows:  $Q = [q_v \ 0; 0 \ q_a I]$ , where  $q_v = 20$  is the penalty for  $v(k)$  and  $q_a = 10$  is the penalty for  $p(k)$ . For the input variables, the penalty matrix is given as  $R = [5 \ 0; 0 \ 15]$ . The constraints on  $y(t)$  are applied at  $\zeta \in [4.75, 5.0]$  cm. This constraint is implemented with  $\alpha = 3$ . Note that this MPC formulation does not include the nonlinear term in (3.1a). However, since this term has a stabilizing effect on the system, this exclusion has no negative effect on the stability of the closed loop system. In the simulation, this nonlinear term is added to the closed loop system as  $\mathcal{G}_n(t) = g(a(\zeta, t)^3, \phi_n^*(\zeta))$ .

The controller action at each time step is computed according to the scheme described in Section 3.3. The control horizon is set to  $N = 300$ , such that the optimization problem is feasible. At time instant  $k$ , a sequence of  $N$  future control moves,  $\bar{u}^N$ , is obtained by solving the quadratic program Eq. 3.21, subject to the inequality and equality constraints presented in Section 3.3.2. This is achieved by using the 'quadprog' function in Matlab. The first element in  $\bar{u}^N$ ,  $\bar{u}(k)$  is then applied to the closed loop system, evolving the state variables. The optimization is then repeated using the updated state variables. The procedure for the implementation in Matlab is as follows:

Starting from  $k = 0$  and the initial condition  $\bar{x}(0)$ ,

1. Compute the matrices  $H$  and  $G$  according to Eq. 3.22, where  $\bar{Q}$  is given by Eq. 3.20.
2. Let  $f = G\bar{x}(k)$
3. For the inequality constraints, write Eq. 3.24 as  $A\bar{u}^N \leq b$ , where  $A$  and  $b$  can be computed according to Eq. 3.25.
4. For the equality constraint, compute  $A_{eq}$  and  $b_{eq}$  according to Eq. 3.26.
5. Solve the quadratic problem given in Eq. 3.21 using the function 'quadprog':

$$\bar{u}^N = \text{quadprog}(H, f, A, b, A_{eq}, b_{eq})$$

6. Since there are two input variables,  $\bar{u}(k) = \bar{u}^N(1:2)$ . That is, the current inputs correspond to the first two elements of  $\bar{u}^N$ .
7. Given  $\bar{x}(k)$  and  $\bar{u}(k)$ , compute  $\bar{x}(k+1)$  according to Eq. 3.14.
8. Let  $k = k+1$  and repeat steps 2 - 7, using the updated state variable. Note that matrices  $H$ ,  $G$ ,  $A$ , and  $A_{eq}$  remain constant for all time steps and therefore can be computed separately.

The closed loop response for  $a(\zeta, t)$  is given in Fig. 3.2. As shown by this figure, stabilization of the alternans from an initial distribution  $a(\zeta, 0) = a_0(\zeta)$  is achieved after approximately 40 beats. Trajectories of  $v(t)$ ,  $u_{Ca}(t)$  and  $y(t)$  are given in Figures 3.3 - 3.5, respectively. For all three variables, constraints satisfaction is achieved.

As mentioned in the previous chapter, an important limitation for the boundary actuator is the fact that the pacing protocol should not postpone the heart's natural rhythm, which is governed by the sinoatrial node (SAN). This means that the boundary actuation is constrained to negative perturbations only. As shown by Figure 3.3, this constraint is indeed satisfied.

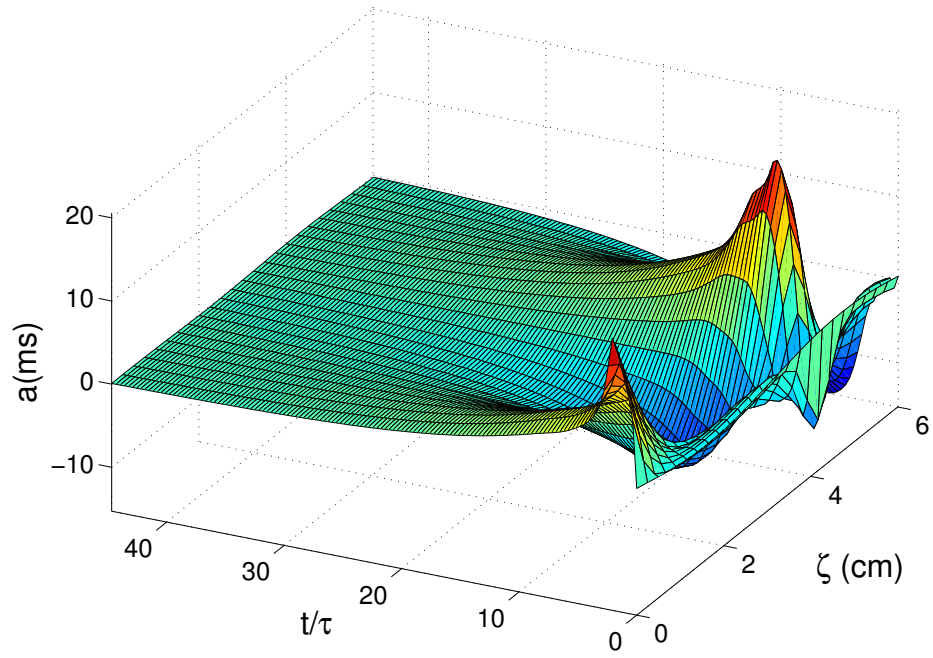


Figure 3.2: Stabilization of the amplitude of alternans PDE with model predictive control

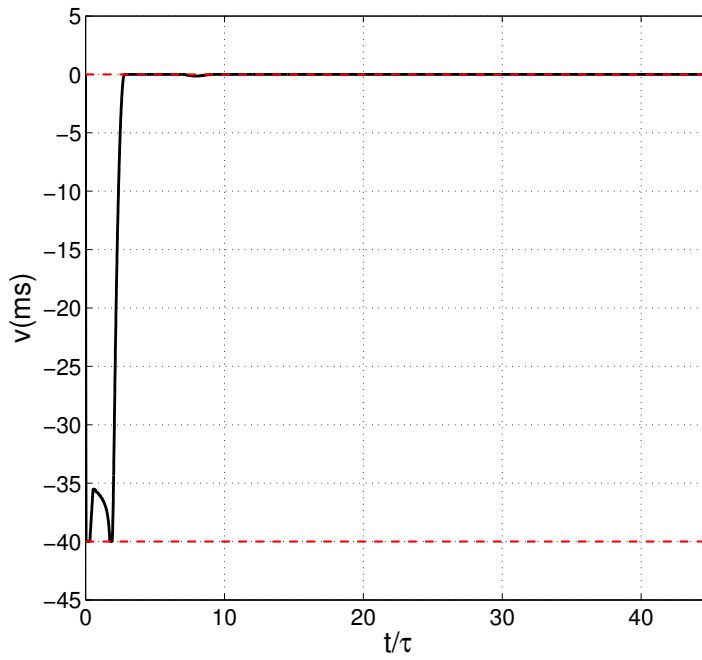


Figure 3.3: Trajectory of  $v(t)$  under model predictive control. Constraints are shown as red dotted lines.

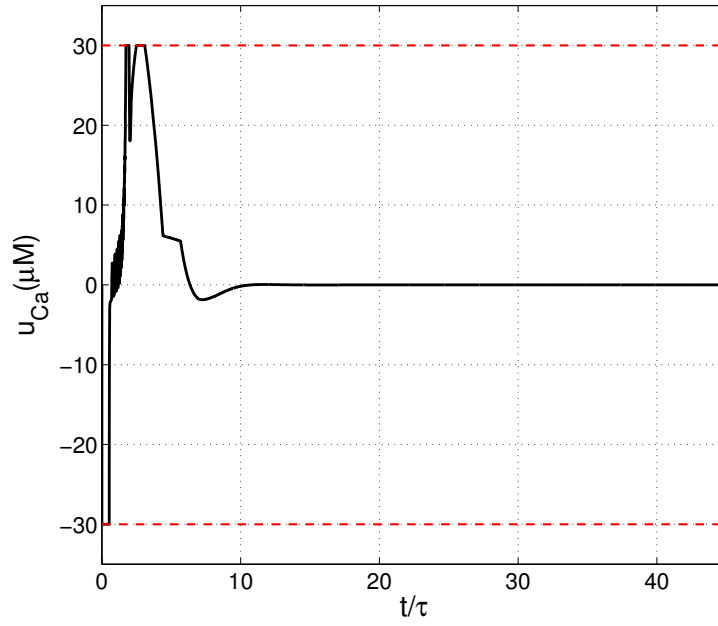


Figure 3.4: Trajectory of  $u_{Ca}(t)$  under model predictive control. Constraints are shown as red dotted lines

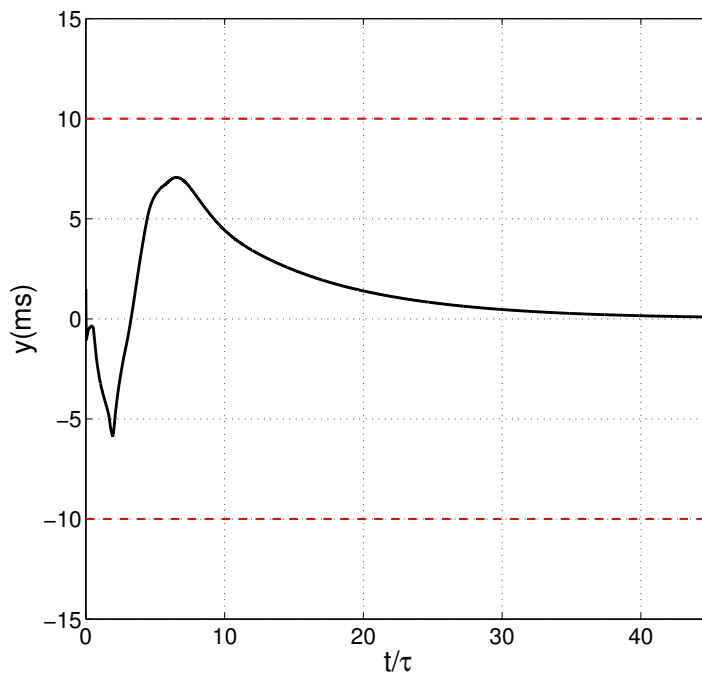


Figure 3.5: Trajectory of  $y(t)$  under model predictive control. Constraints are shown as red dotted lines.

## 3.5 Conclusion

In this chapter, we developed a model predictive controller for the annihilation of cardiac alternans, using a combination of boundary and spatially distributed ( $\text{Ca}^{2+}$ -based) actuators. The dynamics of these alternans along a 1D cable are described by a parabolic PDE, which can be represented as an infinite-dimensional state space system. A low-order, stabilizing MPC that minimizes the infinite horizon cost function was developed based on the discrete-time state space realization of the PDE. Input and state constraints were explicitly accounted for in this approach, which can ensure that these control actions will not induce conduction block in the cardiac tissue. Through numerical simulations, we demonstrated that the low-order MPC can successfully stabilize the entire system, while simultaneously satisfying the input and state constraints imposed on the system. Following these results, the issue of controller robustness with respect to uncertainties in the model parameters need to be addressed, since the PDE parameters can vary significantly depending on the choice of ionic model. This is presented in the next chapter.

## Chapter 4

# Robust model predictive control of the amplitude of alternans PDE

### 4.1 Introduction

In this chapter, we consider the problem of cardiac alternans annihilation using robust model predictive control (MPC). The spatiotemporal dynamics of the cardiac alternans are represented by the small amplitude of alternans PDE [31], and control action is delivered by a boundary actuator and a spatially distributed,  $\text{Ca}^{2+}$ -based actuator. This PDE belongs to a class of parabolic PDEs that describe diffusion-convection-reaction processes, which can be transformed into an infinite dimensional abstract evolutionary form [32, 33].

In Chapter 3, we have demonstrated that MPC can successfully stabilize the amplitude of alternans PDE, thus annihilating the alternans. However, one shortcoming of the traditional MPC techniques is their inability to explicitly account for model uncertainties [46]. In most MPC formulations, the minimization is performed on a nominal cost function, based on a single model of the system. Therefore, when applied to the actual uncertain system, the controller may perform poorly. This motivates the development of robust MPC algorithms, where the controller is designed to account for the model uncertainties, thus ensuring that closed loop stability and other performance criteria can be maintained for the specified range of model uncertainties [46–48]. A review of the various uncertain model descriptions as well as the proposed techniques to satisfy robust constraints handling, stability and controller performance is presented in [47].

In this work, based on the approach used in [40, 41], the infinite dimensional system is partitioned into slow (finite dimensional) and fast (infinite dimensional) subsystems, from which a low order, finite dimensional robust MPC can be constructed using one of the existing robust MPC formulations. The uncertain system is represented as a polytope, and the control objective is to ensure robust stability with input and state constraints satisfaction. In the cardiac system, these

constraints are important for avoiding conduction block in the tissue.

This chapter is organized as follows. The amplitude of alternans PDE and the system's state space representation is introduced in Section 4.2. Section 4.3 is devoted to the robust MPC formulation for a polytopic system. A numerical example is presented in Section 4.4, and a brief summary is provided in Section 4.5.

## 4.2 Model description

The model used in this chapter is identical to that studied in Chapter 3. To summarize, the system to be studied, which is the small amplitude of alternans PDE [31], is given by:

$$\frac{\partial a(\zeta, t)}{\partial t} = \text{Da} \frac{\partial^2 a(\zeta, t)}{\partial \zeta^2} - \omega \frac{\partial a(\zeta, t)}{\partial \zeta} + \sigma a(\zeta, t) - ga(\zeta, t)^3 + h \sum_{j=1}^q b_j(\zeta) u_{Ca_j}(t) \quad (4.1a)$$

$$\frac{\partial a(0, t)}{\partial \zeta} = a(0, t) + v(t), \quad \frac{\partial a(L, t)}{\partial \zeta} = 0 \quad (4.1b)$$

$$a(\zeta, 0) = a_0(\zeta) \quad (4.1c)$$

The system output, which represents the measurement of  $a(\zeta, t)$  at  $\zeta_c$ , is defined as

$$y(t) = \int_0^L r(\zeta) a(\zeta, t) d\zeta \quad (4.2)$$

This system has an infinite dimensional state space system representation, which takes the following form

$$\begin{bmatrix} \dot{v}(t) \\ \dot{p}_n(t) \end{bmatrix} = \begin{bmatrix} 0 & 0 \\ 0 & \lambda_n \end{bmatrix} \begin{bmatrix} v(t) \\ p_n(t) \end{bmatrix} + \begin{bmatrix} 1 & 0 \\ -\langle B, \phi_n^* \rangle & h \langle b, \phi_n^* \rangle \end{bmatrix} \begin{bmatrix} \tilde{v}(t) \\ u_{Ca}(t) \end{bmatrix}, \quad n \geq 1$$

$$\dot{x}(t) = A^e x(t) + B^e u(t) \quad (4.3a)$$

$$y(t) = \begin{bmatrix} \langle r(\zeta), B(\zeta) \rangle & \langle r(\zeta), \phi_n(\zeta) \rangle \end{bmatrix} x(t) = Cx(t), \quad n \geq 1 \quad (4.3b)$$

For the derivation of Eq. 4.3, as well as the detailed definitions of the PDE parameters, refer to Chapters 2 and 3.

For the controller formulation, the system need to be discretized. To ensure that the system's fastest dynamics are not lost during in the discretization, the sampling interval is chosen such that  $\Delta t \leq \frac{1}{2|\lambda_n|_{\max}}$ . To dicretize an infinite dimensional systems, one approach is to employ the Tustin time discretization scheme, which utilizes the Cayley transform [44]. This method is based on a modified Crank-Nicholson type discretization scheme. The discrete-time representation of Eqs. 4.3 is given by:

$$\bar{x}(k+1) = \bar{A}\bar{x}(k) + \bar{B}\bar{u}(k), \quad (4.4a)$$

$$y(k) = C\bar{x}(k) \quad (4.4b)$$

for  $k \geq 0$ . The matrices  $\bar{A}$  and  $\bar{B}$  are defined as follows:

$$\bar{A} = (\mu I - A^e)^{-1}(\mu I + A^e) \quad (4.5)$$

$$\bar{B} = \sqrt{2\mu}(\mu I - A^e)^{-1}B^e \quad (4.6)$$

where  $\mu = \frac{2}{\Delta t}$  and  $I$  is the identity matrix

### 4.2.1 Polytopic model for the uncertain system

The parameters for the PDE given by Eq. 4.1 are derived from the restitution curve, and their values are therefore dependent on the ionic model used to generate the curve. As a result, these parameter values may vary significantly depending on the choice of the ionic model, giving rise to uncertainties in the PDE and its state space representation (Eq. 4.3). A controller that is formulated based on a nominal model may perform very well for that given model, but it may perform poorly in the presence of model uncertainties. It is therefore necessary to consider a robust controller which will satisfy the performance requirements in the presence of model uncertainties. To design such a controller, we first develop a polytopic model to represent the uncertain system.

The parameter uncertainties in the PDE generate a set of linear models that satisfy Eq. 4.4. It is assumed that these uncertain models, denoted by  $\begin{bmatrix} \bar{A}_i & \bar{B}_i \\ C_i & 0 \end{bmatrix}$ , belong to the polytopic set  $\Omega$ , and that the actual (nominal) model lies within this polytope. The polytope  $\Omega$  is defined as

$$\Omega = \text{Co} \left\{ \begin{bmatrix} \bar{A}_1 & \bar{B}_1 \\ C_1 & 0 \end{bmatrix}, \begin{bmatrix} \bar{A}_2 & \bar{B}_2 \\ C_2 & 0 \end{bmatrix}, \dots, \begin{bmatrix} \bar{A}_m & \bar{B}_m \\ C_m & 0 \end{bmatrix} \right\} \quad (4.7)$$

where Co denotes the convex hull, and each  $\begin{bmatrix} \bar{A}_i & \bar{B}_i \\ C_i & 0 \end{bmatrix}$  are the vertices of the convex hull. If  $\begin{bmatrix} \bar{A} & \bar{B} \\ C & 0 \end{bmatrix} \in \Omega$ , then one can find the nonnegative scalars  $\xi_i$  such that

$$\begin{bmatrix} \bar{A} & \bar{B} \\ C & 0 \end{bmatrix} = \sum_{i=1}^m \xi_i \begin{bmatrix} \bar{A}_i & \bar{B}_i \\ C_i & 0 \end{bmatrix}, \quad \sum_{i=1}^m \xi_i = 1 \quad (4.8)$$

## 4.3 Robust model predictive control

In this section, we formulate a robust constrained model predictive controller (MPC) for the set of uncertain models arising from the PDE parameter uncertainties. The robust MPC minimizes the upper bound of a quadratic function, which is expressed as a set of linear matrix inequalities (LMIs). Input and state (output) constraints are also expressed as additional LMIs. In this work,

we are applying the robust MPC formulation developed by Xia et al. [48], which is based on parameter-dependent Lyapunov functions. Compared to the earlier formulation presented in [46], which relies on a single Lyapunov function, this formulation is less conservative. Although the robust MPC in [48] was developed for a finite dimensional systems, here we are applying it on an infinite dimensional system representation.

The eigenspectra of dissipative, parabolic PDEs such as that given by Eq. 4.1a has a beneficial structure which allows for the formulation of a simple control law which stabilizes the unstable modes, while the stable modes remain invariant to the control law. The eigenspectrum of  $\mathcal{A}^e$  can be divided into a finite-dimensional unstable (slow) part and an infinite-dimensional stable (fast) part, i.e.  $\Lambda(\mathcal{A}^e) = \Lambda^+(\mathcal{A}^e) \cup \Lambda^-(\mathcal{A}^e)$ . Since the dominant dynamics of the PDE are captured in the slow subsystem, the finite-dimensional robust MPC is developed based on this subsystem, yielding a stabilizing, low-order robust controller for the entire infinite dimensional system.

Each of the uncertain models in Eq. 4.7 is partitioned into slow and fast subsystems, according to the eigenspectrum of  $\bar{A}_i$ . These subsystems are given by:

$$\bar{x}_s(k+1) = \bar{A}_{i,s}\bar{x}_s(k) + \bar{B}_{i,s}\bar{u}(k) \quad (4.9a)$$

$$\bar{x}_f(k+1) = \bar{A}_{i,f}\bar{x}_f(k) + \bar{B}_{i,f}\bar{u}(k) \quad (4.9b)$$

$$y_s(k) = C_{i,s}\bar{x}_s(k) \quad (4.9c)$$

$$y_f(k) = C_{i,f}\bar{x}_f(k), \quad k \geq 0 \quad (4.9d)$$

In Eqs. 4.9a and 4.9c, the state variables are  $\bar{x}_s(k) = [v(k) \ p_s(k)]'$ , while in Eqs. 4.9b and 4.9d,  $\bar{x}_f(k) = p_f(k)$ . The subscripts  $s$  and  $f$  denote slow and fast modes, respectively.

At each time step, the robust MPC computes a state feedback law that minimizes the following robust performance objective function over an infinite horizon:

$$\min_{\bar{u}(k+j)} \max_{\substack{\bar{A} \\ \bar{B} \in \Omega, j \geq 0}} J_\infty(k) = \sum_{j=0}^{\infty} [\bar{x}_s(k+j)' Q \bar{x}_s(k+j) + \bar{u}(k+j)' R \bar{u}(k+j)] \quad (4.10)$$

where  $Q > 0$  and  $R > 0$  are the symmetric penalty matrices for the state and input variables, respectively. The state feedback law has the form

$$\bar{u}(k+j) = F(k)\bar{x}_s(k+j), \quad j \geq 0 \quad (4.11)$$

where  $F(k)$  is the feedback gain computed at time  $k$ . From this sequence of inputs, only the first control action,  $\bar{u}(k)$ , will be applied to the plant. The minimization is then repeated using the updated state variables.

Since it is difficult to obtain the objective function  $J_\infty(k)$ , the controller is instead designed to minimize an upper bound on  $J_\infty(k)$ . To derive this upper bound, we consider the quadratic

function  $V(\bar{x}_s(k)) = \bar{x}_s(k)'P(\xi)\bar{x}_s(k)$ , where  $P(\xi)$  is a parameter-dependent positive definite matrix.

At sampling time  $k$ , it is assumed that  $V(\bar{x}_s(k))$  satisfies the following inequality for all  $\bar{x}_s(k+j)$ ,

$\bar{u}(k+j)$ ,  $j \geq 0$  satisfying Eq. 4.9a, and for  $\begin{bmatrix} \bar{A} & \bar{B} \\ C & 0 \end{bmatrix} \in \Omega$ :

$$V(\bar{x}_s(k+j+1)) - V(\bar{x}_s(k+j)) \leq -[\bar{x}_s(k+j)'Q\bar{x}_s(k+j) + \bar{u}(k+j)'R\bar{u}(k+j)] \quad (4.12)$$

For the cost function to be finite, as  $j \rightarrow \infty$ ,  $\bar{x}_s(j)$  should approach zero. That is,  $\bar{x}_s(\infty) = 0$ , and therefore  $V(\bar{x}_s(\infty)) = 0$ . Summing Eq. 4.12 from  $j = 0$  to  $j = \infty$  leads to:

$$\max_{[\bar{A} \ \bar{B}] \in \Omega, j \geq 0} J_\infty \leq V(\bar{x}_s(k)) \quad (4.13)$$

$V(\bar{x}_s(k))$  is therefore an upper bound on  $J_\infty$ . Thus, at every sampling time  $k$ , the controller is designed to minimize  $V(\bar{x}_s(k))$ . This problem is then cast as a linear objective minimization problem (LOP), and the following theorem from [48] gives the conditions for the existence of the appropriate  $P(\xi)$  that satisfies Eq. 4.12 and the corresponding feedback gain  $F(k)$ .

**Theorem 1** *If the LOP*

$$\min_{E, V, \hat{P}_i, U_i, Z, H, S} \gamma \quad (4.14a)$$

*subject to the LMIs*

$$\begin{bmatrix} -1 & \bar{x}_s(k)' \\ * & \hat{P}_i - V - V' \end{bmatrix} < 0 \quad (4.14b)$$

$$\begin{bmatrix} -\hat{P}_i & V'\bar{A}'_{i,s} + E'\bar{B}'_{i,s} & E'R & V'Q \\ * & \hat{P}_i - V - V' & 0 & 0 \\ * & * & -\gamma R & 0 \\ * & * & * & -\gamma Q \end{bmatrix} < 0 \quad (4.14c)$$

$$\begin{bmatrix} -Z & E \\ * & -\hat{P}_i \end{bmatrix} < 0, \quad \text{where } Z_{hh} < \bar{u}_{h,\max}^2, \quad h = 1, 2, \dots, q \quad (4.14d)$$

$$\begin{bmatrix} -U_i & \bar{A}_{i,s}V + \bar{B}_{i,s}E \\ * & -\hat{P}_i \end{bmatrix} < 0 \quad (4.14e)$$

$$\begin{bmatrix} -S & C_{i,s}H' \\ * & U_i - H - H' \end{bmatrix} < 0, \quad \text{where } S_{hh} < y_{h,\max}^2, \quad h = 1, 2, \dots, r \quad (4.14f)$$

has the solutions  $E, V, Z, H, \hat{P}_i > 0, U_i > 0 \forall i = 1, 2, \dots, m$ , then the parameter-dependent Lyapunov function can be taken as  $V(\bar{x}_s(k)) = \bar{x}_s(k)'(V')^{-1} \sum_{i=1}^m \xi_i \hat{P}_i V^{-1} \bar{x}_s(k)$  and the state feedback control law is given by  $\bar{u}(k+j) = F(k)\bar{x}_s(k+j)$ ,  $j \geq 0$ , where  $F(k) = EV^{-1}$ . Then:

- i the feasible receding horizon state feedback control law  $\bar{u}(k) = F(k)\bar{x}_s(k)$ ,  $k \geq 0$ , obtained by solving the LOP at each sampling instant robustly asymptotically stabilizes the resulting closed loop system given by Eq. 4.4a.
- ii the upper bound of  $V(\bar{x}_s(k))$  on the robust performance objective function  $J_\infty$  is minimized at sampling time  $k$ .
- iii the component-wise peak bound on  $\bar{u}_h(k+j)$  satisfies

$$|\bar{u}_h(k+j)| \leq \bar{u}_{h,\max}, \quad j \geq 0, \quad h = 1, 2, \dots, q \quad (4.15)$$

- iv the component-wise peak bound on  $y_h(k+j)$  satisfies

$$|y_h(k+j)| \leq y_{h,\max}, \quad j \geq 0, \quad h = 1, 2, \dots, r \quad (4.16)$$

The proof for this theorem can be found in the original work [48]. Note that LMIs in Theorem 1 are constructed based only on the slow subsystem (Eqs. 4.9a and 4.9c). However, since the fast subsystem (Eqs. 4.9b and 4.9d) is stable and  $\bar{x}_f(j) \rightarrow 0$  as  $j \rightarrow \infty$ , the feedback law obtained by solving the LOP is able to stabilize the entire infinite dimensional system given by Eq. 4.4.

## 4.4 Numerical Simulation

In this simulation study, we consider the PDE given by Eq. 4.1 with parameters obtained from the Fox ionic model [35]. The nominal values for these parameters are as follows:  $Da = 0.148$ ,  $\omega = 0.04$ ,  $\sigma = \ln(1.314)$ ,  $g = 7.221 \times 10^{-5}$  and  $h = 0.6$ . A cable length of 6.25 cm is used in the simulation.

For the uncertain models we consider a  $\pm 40\%$  uncertainty on  $Da$ ,  $\omega$  and  $\sigma$ . In order to make sure that the eigenfunctions are the same for each set of parameters,  $Da$  and  $\omega$  must be varied at the same time. This means that the polytope given by Eq. 4.7 can be made up of up to four uncertain models. The possible combinations are given in Table 4.1. Initially, the polytope was constructed using all four uncertain models. However, it was found that to satisfy the condition given by Eq. 4.8,  $\xi_3 = \xi_4 = 0$ . Thus, only the first two uncertain models are considered (i.e.,  $m = 2$ ).

The Galerkin formulation for  $p(\zeta, t)$  is approximated using 44 modes, namely  $p(\zeta, t) \simeq \sum_{n=1}^{44} p_n(t)\phi_n(\zeta)$ . This leads to the finite dimensional approximation to Eq. 4.3a, where the extended state variable  $x(t)$  has 45 elements. The function  $B(\zeta)$  has the general form

$$B(\zeta) = \exp^{a\zeta} [c_1 \cos(b\zeta) + c_2 \sin(b\zeta)]$$

Table 4.1: Combination of parameters for the uncertain models, in terms of deviation from the nominal values

$i$	Da	$\omega$	$\sigma$
1	+40%	+40%	+40%
2	-40%	-40%	-40%
3	+40%	+40%	-40%
4	-40%	-40%	+40%

where  $a$  and  $b$  are the real and imaginary parts of  $r$ , which satisfy the characteristic equation of Eq.3.1a:

$$Dar^2 - \omega r + \sigma = 0$$

The coefficients  $c_1$  and  $c_2$  can be found by applying the following boundary conditions:

$$\frac{dB}{d\zeta} \Big|_{\zeta=0} - B(0) = 1 \quad \frac{dB}{d\zeta} \Big|_{\zeta=L} = 0$$

One  $\text{Ca}^{2+}$ -based controller,  $u_{Ca}(t)$ , is applied at  $\zeta \in [3.5, 4.0]$  cm.

Once the finite-dimensional approximation for each system has been obtained, they are discretized and decomposed into stable (fast) and unstable (slow) subsystems. The low-dimensional slow subsystems are then used in the robust MPC synthesis. The sampling time for the discretization is computed as  $\Delta t = 0.005$ . For all of the uncertain models and a cable length of 6.25 cm,  $\bar{A}_i$ ,  $i = \{1, 2\}$  has two unstable eigenvalues. For the extended state space system, there is an additional zero eigenvalue, which also need to be stabilized. The number of slow modes was chosen to be five. The state penalty matrix can be partitioned as follows:  $Q = [q_v \quad 0; 0 \quad q_a I]$ , where  $q_v = 1$  is the penalty for  $v(k)$  while  $q_a = 0.5$  is the penalty for  $p_s(k)$ . For the input variables, the penalty matrix is given as  $R = [5 \quad 0; 0 \quad 0.1]$ . The constraints on  $y(t)$  are applied at  $\zeta \in [4.0, 4.25]$  cm. Note that the robust MPC formulation does not include the nonlinear term in Eq. 4.1a. However, since this term has a stabilizing effect on the system, this exclusion has no negative effect on the stability of the closed loop system. In the simulation, this nonlinear term is added to the closed loop system as  $\mathcal{G}_n(t) = g\langle a(\zeta, t)^3, \phi_n^*(\zeta) \rangle$ .

At each time step, the feedback gain that minimizes the robust performance objective function is computed according to the scheme described in Theorem 1. Constraints are applied on  $u_{Ca}(k)$ ,  $v(k)$  and  $y(k)$ . Note that in the extended state space,  $v(k)$  is a state variable. Thus the constraint on  $v(k)$  is implemented as a state (output) constraint. The system of LMIs are solved in Matlab using the LMI solvers in the Robust Control Toolbox. To solve the LOP in Matlab, the procedure is:

At  $k = 0$ , given the initial state  $\bar{x}(0)$ ,

1. Initiate the system of LMIs using the function '*setlmis*'.
2. Define the LMI parameters  $\gamma$ ,  $E$ ,  $V$ ,  $\hat{P}_i$ ,  $U_i$ ,  $Z$ ,  $H$  and  $S$  using the function '*lmivar*', for  $i = 1, 2, \dots, m$ .
3. For each  $i$ , define the LMIs given by Eqs. 4.14b - 4.14f using the function '*lmiterm*'.
4. Define the system of LMIs containing all the individual LMIs using the function '*getlmis*'.
5. To solve the LOP, we use the function '*mincx*', which minimizes the function  $c' * x$  subject to the LMIs, where  $x$  is a vector of all the decision variables, which are the free scalar variables in each LMI variable. These variables are sorted according to the order in which the LMI variable is defined in step 2. Since only  $\gamma$  is being minimized, the only entry in  $c$  that is nonzero is the one that corresponds to  $\gamma$ , and this entry is equal to 1.
6. Once the minimization is complete, the decision variables must be converted to matrix variables. This is achieved using the function '*dec2mat*'. The relevant LMI variables are  $E$  and  $V$ .
7. Compute  $F(k) = EV^{-1}$ , and  $\bar{u}(k)$  according to the feedback law in Eq. 4.11. Apply  $\bar{u}(k)$  to Eq. 4.4 to obtain  $\bar{x}(k+1)$ .
8. Let  $k = k + 1$  and repeat steps 1 - 7, using the updated value of  $\bar{x}_s(k)$  in the LMI definition.

The resulting closed loop response for  $a(\zeta, t)$  is given in Figure 4.1. As shown by this figure, the low order feedback control law is able to stabilize the entire high dimensional system after approximately 60 beats. The corresponding trajectories of  $v(t)$ ,  $u_{Ca}(t)$  and  $y(t)$  are shown in Figures 4.2 - 4.4. For clarity, only one of the bounds is shown for  $v(t)$  and  $y(t)$ . As shown by these three figures, all constraints are satisfied.

The stabilization is achieved using the combination of boundary and spatially distributed,  $Ca^{2+}$ -based actuators. The inclusion of the  $Ca^{2+}$ -based actuator, which is voltage-independent, allows us to overcome the controllability limitation encountered by previous control efforts which rely solely on boundary actuation. The inclusion of model uncertainty in the controller design is important, since the PDE parameter values may vary widely depending on the choice of ionic model. As shown by Figures 4.3 - 4.4, the variables  $u_{Ca}(t)$  and  $y(t)$  remains well within their constraints. This suggests that the robust MPC algorithm is still relatively conservative.

It is worth noting that this robust MPC algorithm, along with most of the other existing algorithms, is only able to handle symmetrical constraints. This poses a problem for the boundary actuation  $v(t)$ . As mentioned in previous chapters, the boundary actuation is constrained to negative perturbations only, because the pacing protocol cannot postpone the heart's natural rhythm,

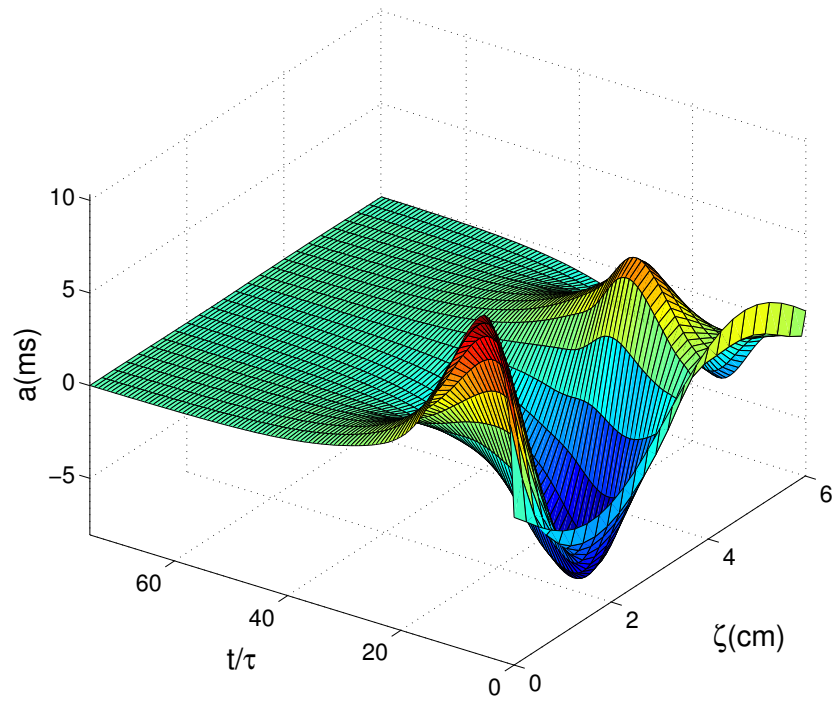


Figure 4.1: Stabilization of the amplitude of alternans PDE under robust MPC.

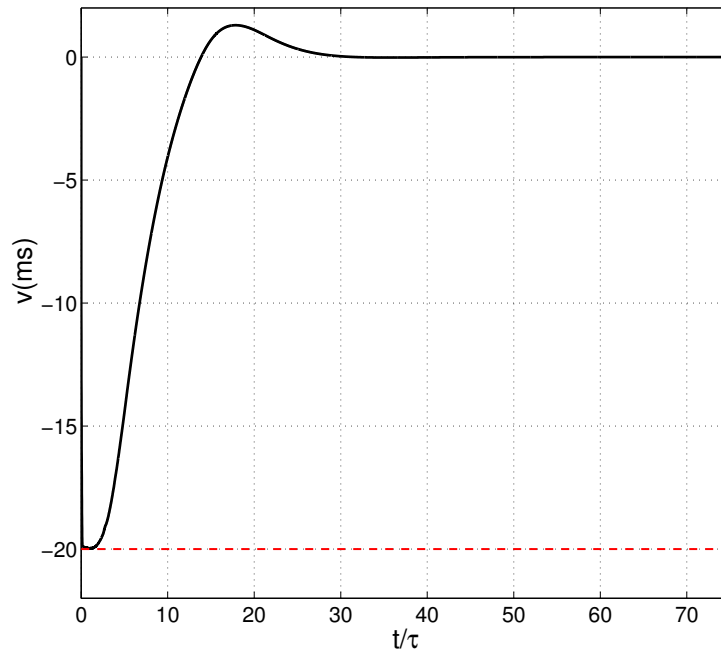


Figure 4.2: Trajectory of the boundary input  $v(t)$ . The red dotted line depicts the lower bound on  $v(t)$ .

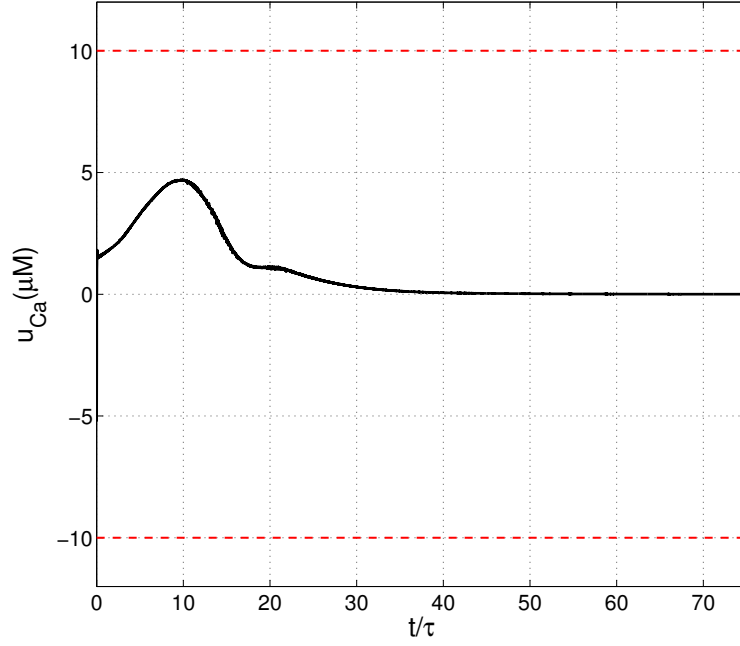


Figure 4.3: Trajectory of  $u_{Ca}(t)$ . Constraints are shown as red dotted lines

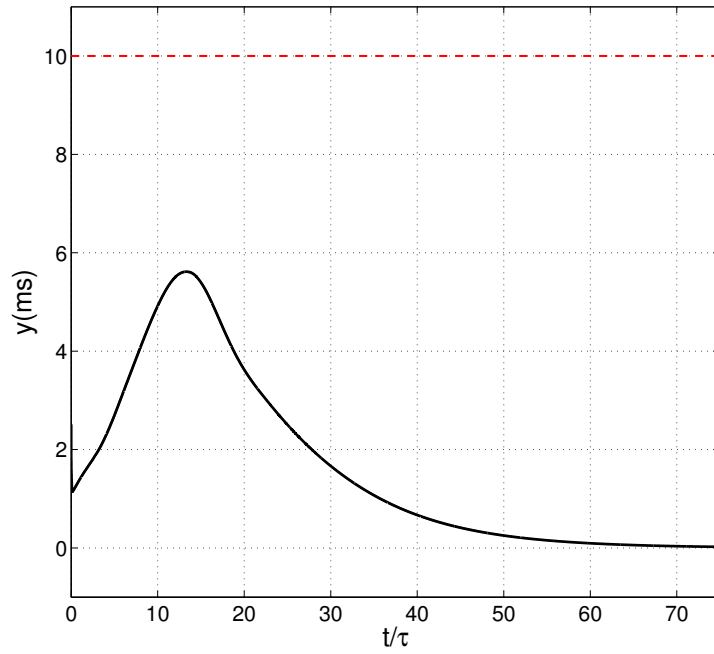


Figure 4.4: Trajectory of  $y(t)$ , which is  $a(\zeta, t)$  measured at  $\zeta_c = 4.125$  cm. The upper bound on  $y(t)$  is shown as a red dotted line.

which is governed by the sinoatrial node (SAN). As can be seen from Figure 4.2, this constraint is violated for a short period of time.

## 4.5 Conclusion

In this chapter, we demonstrated the annihilation of cardiac alternans along a 1D cable of cardiac cells through the application of a robust model predictive control strategy. The dynamics of these alternans are described by a parabolic PDE, with parameters obtained from the Fox ionic model. This PDE was then represented as an infinite-dimensional state space system. A low-order, stabilizing robust MPC that minimizes the robust performance objective function was developed based on the discrete-time state space realization of the PDE, with a  $\pm 40\%$  uncertainty in the PDE parameters. Through numerical simulations, it was shown that the low-order robust MPC can successfully stabilize the entire system, while simultaneously satisfying the input and state constraints. In future work, the robust controller's ability to handle asymmetrical constraints should be addressed to make sure that the computed control actions will not result in conduction block.

## Chapter 5

# Conclusions and future work

### 5.1 Conclusions

In this thesis, the model-based annihilation of cardiac alternans through the combination of a boundary actuator and a spatially distributed,  $\text{Ca}^{2+}$ -based actuator is studied. Three different control strategies were considered, namely optimal full state feedback control, model predictive control and robust model predictive control. The effectiveness of each control strategy was demonstrated through numerical simulations.

Through this work, we have shown that by combining the two types of actuation, we can achieve alternans annihilation in cardiac cables that are 6.25 cm long. This is a significant contribution, since many previous research efforts that relied solely on boundary actuation could only stabilize alternans in cardiac cables that are  $\approx 1$  cm long. Thus, by applying our control strategy, the controllability limitation that has been encountered by many previous researchers can be overcome.

In Chapter 2, an optimal full state feedback controller was developed for the coupled system of PDEs. The first PDE describes the dynamics of the APD alternans, while the second PDE describes the dynamics of the alternations in the peak  $\text{Ca}^{2+}$  concentration. In deriving the PDE parameters, two ionic modes were considered, namely the LR1 model and the Fox model. For the LR1 model, the coupling between the PDEs was unidirectional ( $V \rightarrow \text{Ca}^{2+}$ ). On the other hand, for the Fox model, the coupling was bidirectional. By analyzing the eigenspectra of each individual PDE, it was revealed that on its own, the Calcium dynamics is stable. As a result, in the case where the coupling is unidirectional, only the APD alternans need to be stabilized, and this was achieved through boundary actuation only. On the other hand, in the case where coupling is bidirectional, both systems need to be stabilized. Although our simulation results for the LR1 model show that alternans annihilation along a 6.25 cm cable can be achieved through boundary control alone, experimental results have proved otherwise. Therefore, in simulating the control strategy, it is important to choose an ionic model where the coupling between voltage and calcium

dynamics are adequately represented.

In working with the cardiac system, one must be careful to not violate constraints that are naturally present. One such constraint is the fact that the boundary actuator, which represents a pacing protocol, should not be allowed to delay the heart's natural rhythm. In other words, the boundary actuator can only take on negative values. With this in mind, a model predictive controller (MPC) was developed in Chapter 3. In this chapter, only the amplitude of APD alternans PDE was considered. Within the MPC framework, constraints can be explicitly accounted for in the controller formulation. Through simulations, using parameters obtained from the Fox model, we demonstrated that the low order MPC is able annihilate alternans along the entire cable, while making sure that input and state constraints are satisfied.

For the same system, a robust MPC was also developed in Chapter 4. Since the PDE parameters were obtained from an ionic model, their values can vary greatly depending on the choice of ionic model. Therefore, it is important to find a controller that can still achieve closed loop stabilization and constraints satisfaction in the presence of model uncertainties. In this approach, the uncertain models are assumed belong to a polytope, and an LMI-based optimization was performed at each time step to determine the optimum feedback law. Our simulation results show that although the controller is relatively conservative, this robust MPC formulation can indeed achieve closed loop stabilization and constraints satisfaction for the given range of model uncertainties.

## 5.2 Future work

One natural extension to the work in this thesis is the development of an output feedback controller, in which measurements of the alternans at discrete points along the cable are used to reconstruct their profiles along the entire cable. The estimated profile will then be used to compute the control action. As shown in [22], if an unstable mode is unobservable, feedback control will not be able to suppress it. Therefore, the number of sensors must be equal to or greater than the number of unstable modes in the system. For a cable length of 6.25 cm, there are two unstable eigenvalues (excluding the zero eigenvalue), so at least two sensors are required for a proper observer design. This is convenient, since the sensors can be placed at either end of the cable. As the number of unstable eigenvalues increases with the cable length, more sensors will be required for longer cables.

For the  $\text{Ca}^{2+}$ -based actuator, modulating the intracellular  $\text{Ca}^{2+}$  concentration affects the tissue's mechanical properties. In general, however,  $[\text{Ca}^{2+}]$  is a weak modulator for the heart's mechanical activities compared to a direct mechanical stimulus. Furthermore, measurements of the intracellular  $\text{Ca}^{2+}$  concentration may not be readily available. Therefore, it will be beneficial to have a control scheme in which the feedback algorithm applies direct mechanical perturbations to

the cable. This can be achieved through the three variable Nash-Panfilov model [49].

As mentioned in Chapter 4, the robust MPC formulation here can only handle symmetrical constraints. In order to strictly enforce the constraint on the boundary actuation, the formulation will need to be modified such that asymmetrical constraints can also be applied.

Finally, another possible extension of the work presented in this thesis is to apply the control strategies to two (or three) dimensional cardiac tissues.

# Bibliography

- [1] V. L. Rogers *et al.*, “Heart disease and stroke statistics - 2012 update: report from the american heart association,” *Circulation*, vol. 125, pp. e2 – e220, 2012.
- [2] G. E. Billman, “Cardiac autonomic neural remodeling and susceptibility to sudden cardiac death: effect of endurance exercise training,” *Am. J. Physiol. Heart Circ. Physiol.*, vol. 297, no. 4, pp. H1171 – H1193, 2009.
- [3] A. Burke and R. Virmani, “Sudden natural death | cardiovascular,” in *Encyclopedia of Forensic and Legal Medicine* (J. Payne-James, ed.), pp. 211 – 223, Oxford: Elsevier, 2005.
- [4] J. M. Pastore, S. D. Girouard, K. R. Laurita, F. G. Akar, and D. S. Rosenbaum, “Mechanism linking t-wave alternans to the genesis of cardiac fibrillation,” *Circulation*, vol. 99, pp. 1385 – 1394, 1999.
- [5] S. M. Narayan, “T-wave alternans and human ventricular arrhythmias: What is the link?,” *J. Am. Coll. Cardiol.*, vol. 49, no. 3, pp. 347 – 349, 2007.
- [6] J.-M. Cao *et al.*, “Spatiotemporal heterogeneity in the induction of ventricular fibrillation by rapid pacing : Importance of cardiac restitution properties,” *Circ. Res.*, vol. 84, no. 11, pp. 1318 – 1331, 1999.
- [7] D. S. Rosenbaum, L. E. Jackson, J. M. Smith, H. Garan, J. N. Ruskin, and R. J. Cohen, “Electrical alternans and vulnerability to ventricular arrhythmias,” *New Engl. J. Med.*, vol. 330, no. 4, pp. 235 – 241, 1994.
- [8] A. Karma, “Electrical alternans and spiral wave breakup in cardiac tissue,” *Chaos*, vol. 4, no. 3, pp. 461 – 472, 1994.
- [9] J. N. Weiss, A. Garfinkel, H. S. Karagueuzian, Z. Qu, and P. S. Chen, “Chaos and the transition to ventricular fibrillation,” *Circulation*, vol. 99, pp. 2819 – 2826, 1999.
- [10] J. Keener and J. Sneyd, *Mathematical Physiology*. New York: Springer-Verlag, 1998.

- [11] Y. Shiferaw, D. Sato, and A. Karma, “Coupled dynamics of voltage and calcium in paced cardiac cells,” *Phys. Rev. E*, vol. 71, no. 2, p. 021903, 2005.
- [12] Y. Shiferaw and A. Karma, “Turing instability mediated by voltage and calcium diffusion in paced cardiac cells,” *PNAS*, vol. 103, no. 15, pp. 5670 – 5675, 2006.
- [13] D. Sato, Y. Shiferaw, A. Garfinkel, J. N. Weiss, Z. Qu, and A. Karma, “Spatially discordant alternans in cardiac tissue - role of calcium cycling,” *Circ. Res.*, vol. 99, no. 5, pp. 520 – 527, 2006.
- [14] D. J. Christini, M. L. Riccio, C. A. Culianu, J. J. Fox, A. Karma, and R. F. Gilmour Jr., “Control of electric alternans in canine cardiac purkinje fibers,” *Phys. Rev. Lett.*, vol. 96, no. 10, p. 104101, 2006.
- [15] J. J. Fox, M. L. Riccio, F. Hua, E. Bodenschatz, and R. F. Gilmour Jr., “Spatiotemporal transition to conduction block in canine ventricle,” *Circ. Res.*, vol. 90, no. 3, pp. 289 – 296, 2002.
- [16] S. Sridhar, D. M. Le, Y. C. Mi, S. Sinha, P. Y. Lai, and C. K. Chan, “Suppression of cardiac alternans by alternating-period-feedback stimulations,” *Phys. Rev. E*, vol. 87, p. 042712, 2013.
- [17] B. Echebarria and A. Karma, “Spatiotemporal control of cardiac alternans,” *Chaos*, vol. 12, no. 3, pp. 923 – 930, 2002.
- [18] T. Krogh-Madsen, A. Karma, M. L. Riccio, P. N. Jordan, C. D. J., and R. F. Gilmour Jr., “Off-site control of repolarization alternans in cardiac fibers,” *Phys. Rev. E*, vol. 81, no. 1, p. 011915, 2010.
- [19] S. Dubljevic, S. F. Lin, and P. D. Christofides, “Studies on feedback control of cardiac alternans,” *Comput. Chem. Eng.*, vol. 32, no. 9, pp. 2086 – 2098, 2008.
- [20] S. F. Lin and S. Dubljevic, “Pacing real-time spatiotemporal control of cardiac alternans,” in *Proceedings of the 2007 American Control Conference*, pp. 600 – 606, IEEE, 2007.
- [21] A. Garzon, R. O. Grigoriev, and F. H. Fenton, “Model-based control of cardiac alternans on a ring,” *Phys. Rev. E*, vol. 80, no. 2, p. 021932, 2009.
- [22] A. Garzon, R. O. Grigoriev, and F. H. Fenton, “Model-based control of cardiac alternans in purkinje fibers,” *Phys. Rev. E*, vol. 84, no. 4, p. 041927, 2011.

- [23] S. H. Weinberg and L. Tung, “Oscillation in cycle length induces transient discordant and steady-state concordant alternans in the heart,” *PLoS ONE*, vol. 7, no. 7, p. e40477, 2012.
- [24] H. Dvir and S. Zlochiver, “Stochastic cardiac pacing increases ventricular electrical stability - a computational study,” *Biophys. J.*, vol. 105, pp. 533 – 542, 2013.
- [25] D. M. Bers, *Excitation-Contraction Coupling and Cardiac Contractile Force*. The Netherlands: Kluwer Academic Publishers, 2 ed., 2001.
- [26] P. J. Hunter, A. D. McCulloch, and H. E. D. J. ter Keurs, “Modelling the mechanical properties of cardiac muscle,” *Prog. Biophys. Mol. Biol.*, vol. 69, pp. 289 – 331, 1998.
- [27] P. Kohl, P. J. Hunter, and D. Noble, “Stretch-induced changes in heart rate and rhythm: clinical observations, experiments and mathematical models,” *Prog. Biophys. Mol. Biol.*, vol. 82, pp. 91 – 138, 1999.
- [28] O. E. Solovyova, N. A. Vikulova, P. V. Konovalov, P. Kohl, and V. S. Markhasin, “Mathematical modeling of mechano-electric feedback in cardiomyocytes,” *Russ. J. Numer. Anal. Math. Modelling*, vol. 4, pp. 331 – 351, 2004.
- [29] D. M. Bers, “Cardiac excitation-contraction coupling,” *Nature*, vol. 415, pp. 198 – 205, 2002.
- [30] S. C. Calaghan, A. Belus, and E. White, “Do stretch-induced changes in intracellular calcium modify the electrical activity of cardiac muscle?,” *Prog. Biophys. Mol. Biol.*, vol. 82, pp. 81 – 95, 2003.
- [31] B. Echebarria and A. Karma, “Instability and spatiotemporal dynamics of alternans in paced cardiac tissue,” *Phys. Rev. Lett.*, vol. 80, no. 22, p. 208101, 2002.
- [32] R. F. Curtain and H. J. Zwart, *An Introduction to Infinite-Dimensional Linear Systems Theory*. New York: Springer-Verlag, 1995.
- [33] W. H. Ray, *Advanced Process Control*. New York: McGraw-Hill, 1981.
- [34] S. Dubljevic and P. D. Christofides, “Optimal mechano-electric stabilization of cardiac alternans,” *Chem. Eng. Sci.*, vol. 63, no. 22, pp. 5425 – 5433, 2008.
- [35] J. J. Fox, J. L. McHarg, and R. F. Gilmour Jr., “Ionic mechanism of electrical alternans,” *Am. J. Physiol. Heart Circ. Physiol.*, vol. 282, no. 2, pp. H516 – H530, 2002.
- [36] C. H. Luo and Y. Rudy, “A model of the ventricular cardiac action potential. depolarization, repolarization and their interaction,” *Circ. Res.*, vol. 68, pp. 1501 – 1526, 1991.

- [37] C. E. Garcia, D. M. Prett, and M. Morari, “Model predictive control: Theory and practice - a survey,” *Automatica*, vol. 25, no. 3, pp. 335 – 348, 1989.
- [38] K. R. Muske and J. B. Rawlings, “Model predictive control with linear models,” *AIChE J.*, vol. 39, no. 2, pp. 262 – 287, 1993.
- [39] P. D. Christofides, R. Scattolini, D. M. de la Pena, and J. Liu, “Distributed model predictive control: A tutorial review and future research directions,” *Comput. Chem. Eng.*, vol. 51, pp. 21 – 41, 2013.
- [40] S. Dubljevic, N. H. El-Farra, P. Mhaskar, and P. D. Christofides, “Predictive control of parabolic pdes with state and control constraints,” *Int. J. Robust Nonlinear Control*, vol. 16, pp. 749 – 772, 2006.
- [41] S. Dubljevic and P. D. Christofides, “Boundary predictive control of parabolic pdes,” in *Proceedings of the 2006 American Control Conference*, pp. 49 – 56, IEEE, 2006.
- [42] I. Bonis, W. Xie, and C. Theodoropoulos, “A linear model predictive control algorithm for nonlinear large-scale distributed parameter systems,” *AIChE J.*, vol. 58, no. 3, 2012.
- [43] M. J. Tippett and J. Bao, “Distributed model predictive control based on dissipativity,” *AIChE J.*, vol. 59, no. 3, pp. 787 – 804, 2013.
- [44] V. Havu and J. Malinen, “The cayley transform as a time discretization scheme,” *Numer. Func. Anal. Opt.*, vol. 28, no. 7-8, pp. 825 – 851, 2007.
- [45] N. Besseling, *Stability analysis in continuous and discrete time*. PhD thesis, Dept. of Applied Mathematics, Univ. of Twente, Netherlands, 2011.
- [46] M. V. Kothare, V. Balakrishnan, and M. Morari, “Robust constrained model predictive control using linear matrix inequalities,” *Automatica*, vol. 32, no. 10, pp. 1361 – 1379, 1996.
- [47] A. Bemporad and M. Morari, “Robust model predictive control: A survey,” in *Robustness in identification and control*, pp. 207 – 226, Springer, 1999.
- [48] Y. Xia, G. P. Liu, P. Shi, J. Chen, and D. Rees, “Robust constrained model predictive control based on parameter-dependent lyapunov functions,” *Circuits Syst. Signal Process.*, vol. 27, pp. 429 – 446, 2008.
- [49] M. P. Nash and A. V. Panfilov, “Electromechanical model of excitable tissue to study reentrant cardiac arrhythmias,” *Prog. Biophys. Mol. Bio.*, vol. 85, pp. 501 – 522, 2004.